A&A, 715, A128 (2026)
https://doi.org/10.1051/0004-6361/202660650
© The Authors 2026

Astronomy & Astrophysics

Coupling between stellar and HI lopsidedness in Milky Way–type galaxies from the Auriga Superstars cosmological simulations

Arianna Dolfi[1,⋆], Facundo A. Gómez[1], Rebekka Bieri[2], Francesca Fragkoudi[3], Robert J. J. Grand[4], Antonela Monachesi[1], Ruediger Pakmor[6], and Freeke van de Voort[5]

[1] Departamento de Astronomía, Universidad de La Serena, Av. Raúl Bitrán 1305, La Serena, Chile
[2] Universität Zürich, Institut für Astrophysik, Winterthurerstrasse 190, 8057 Zürich, Switzerland
[3] Institute for Computational Cosmology, Department of Physics, Durham University, South Road, Durham DH1 3LE, UK
[4] Astrophysics Research Institute, Liverpool John Moores University, 146 Brownlow Hill, Liverpool L3 5RF, UK
[5] Cardiff Hub for Astrophysics Research and Technology, School of Physics and Astronomy, Cardiff University, Queen's Buildings, Cardiff CF24 3AA, UK
[6] Max-Planck-Institut für Astrophysik, Karl-Schwarzschild-Str. 1, D-85748 Garching, Germany

Received 28 April 2026 / Accepted 13 September 2026

ABSTRACT

Context. Lopsidedness is a common feature in disk galaxies, but its origin and evolution remain poorly understood. Previous works have generally focused on stellar or gas lopsidedness separately. However, a combined analysis can help identify the mechanisms driving lopsidedness and constrain recent galactic evolution and environmental interactions.
Aims. We study lopsidedness in the density and kinematics of the stellar and atomic hydrogen (HI) components of nine Milky Way-type galaxies from the Auriga Superstars cosmological zoom-in simulations. The high stellar mass resolution ($m_* = 800\,M_\odot$) of the simulations improves the visibility of features in the stellar disk and halo, reduces the effect of noise on the measurement of lopsidedness, and provides a refined sampling of the gravitational potential.
Methods. We quantified morphological and kinematical lopsidedness through the amplitude of the first Fourier mode ($m = 1$) of the face-on projected mass distribution and radial velocity maps consistently for stars and gas and over 0.5–1 R_{opt}, where R_{opt} is the stellar optical radius.
Results. At $z = 0$, the morphological lopsidedness of the old stellar component (>0.5 Gyr old) strongly correlates with that of HI, tracing distortions in the global gravitational potential, while the young stellar population (<0.5 Gyr old) primarily traces asymmetric star formation along strong spiral arms. Morphological and kinematical lopsidedness are strongly correlated in stars but weakly correlated in HI, which typically exhibits stronger kinematical asymmetries. We also find that stellar disk lopsidedness is anticorrelated with bar strength, with strongly barred galaxies hosting more symmetric disks and higher central stellar mass densities. Based on our simulations of lopsidedness evolution over the past 7 Gyr, we observed that tidal interactions with massive satellites (mass ratio >1:50) produce coherent lopsided responses in stars and HI. In contrast, smooth gas accretion primarily drives lopsidedness in HI and young stars, while the total stellar component remains largely symmetric. Individual galaxies often experience multiple mechanisms, producing complex coupling and decoupling among distinct tracers.

Key words. galaxies: evolution – galaxies: interactions – galaxies: kinematics and dynamics – galaxies: spiral – galaxies: structure

1. Introduction

Disk galaxies often display asymmetric mass and light distribution (known as lopsidedness; (Baldwin et al. 1980)) such that the outer regions are more extended on one side than on the opposite side. Lopsidedness is also observed in the kinematics, where the rotation curve rises more steeply on one side of the galaxy than on the opposite one. Observational studies have shown that both in the local Universe and at high-redshift (i.e., $z \lesssim 3$), at least one-third of the galaxies have lopsided stellar disks (Zaritsky & Rix 1997; Bournaud et al. 2005; Le Bail et al. 2024). Lopsidedness is not only observed in the spatial distribution of the old stellar component traced in the near-infrared (Block et al. 1994; Rix & Zaritsky 1995) but also in both the spatial distribution and kinematics of atomic hydrogen gas, i.e., HI (Richter & Sancisi 1994; Schoenmakers et al. 1997; Haynes et al. 1998; Swaters et al. 1999). Specifically, Richter & Sancisi (1994) found that at least 50% of galaxies show strong asymmetries in their global HI velocity profiles, caused by intrinsically asymmetric gas distributions and/or kinematics (i.e., an asymmetry in the global HI profile can result from a lopsided spatial distribution and/or lopsided kinematics). Since lopsidedness is stronger at larger radii, it is not surprising that a larger fraction of lopsided galaxies is identified in HI, which is more extended than the stellar component.

Despite lopsidedness being a common phenomenon in galactic disks, its origin and evolution are still not well understood. One of the main processes proposed to explain the origin of lopsidedness are tidal interactions (Beale & Davies 1969; Weinberg 1995), which can generate strong but relatively short-lived lopsided perturbations lasting no more than ∼2 Gyr (Ghosh et al. 2025). These interactions are expected to play a significant role in producing disk asymmetries, particularly in galaxy groups, where encounters are frequent and relative velocities are lower than in clusters. Indeed, observations have shown that early-type disk galaxies in galaxy groups tend to be

⋆ Corresponding author: arianna.dolfi@userena.cl

Open Access article, published by EDP Sciences, under the terms of the Creative Commons Attribution License (https://creativecommons.org/licenses/by/4.0), which permits unrestricted use, distribution, and reproduction in any medium, provided the original work is properly cited.
This article is published in open access under the Subscribe to Open model. Subscribe to A&A to support open access publication.

more lopsided than late-type counterparts (Angiras et al. 2006, 2007). This is consistent with an environmental origin for the early-type galaxy population in groups driven by tidal interactions, which can heat the stellar disk and produce multiple star-bursting episodes, ultimately transforming a gas-rich spiral galaxy into a gas-poor lenticular galaxy (Bournaud et al. 2004; Bekki & Couch 2011; Deeley et al. 2021). However, the observed lack of correlation between lopsidedness and the presence of nearby satellite galaxies in the field (Bournaud et al. 2005; Wilcots 2010), together with the finding that late-type disk galaxies in the field are generally more lopsided in their stellar density distribution than early-type disk galaxies (Bournaud et al. 2005), suggests that additional processes must also be at play. For this reason, subsequent studies have proposed that lopsidedness can arise as a result of the disk response to a previously tidally perturbed dark matter halo (Weinberg 1995; Jog 1997, 2002) or from torques acting as a result of an off-centered disk with respect to the dark matter halo (Noordermeer et al. 2001). Alternatively, Bournaud et al. (2005) suggested that asymmetric gas accretion is the dominant origin of lopsidedness in field galaxies.

Using cosmological simulations from the IllustrisTNG project, Łokas (2022) showed that lopsided galaxies tend to be characterized by higher star formation rates, bluer colors, lower metallicity, and a higher gas fraction than symmetric galaxies at $z = 0$, consistent with the asymmetric gas accretion scenario. Similar conclusions were also reached by Dolfi et al. (2025), who showed that lopsided galaxies have typically experienced more significant recent net gas accretion rates onto their galactic disk than symmetric galaxies. This is also consistent with the finding that lopsided galaxies have a distinct star formation history with respect to their symmetric counterparts at $z = 0$ (Dolfi et al. 2023). They are characterized by a steadier mass growth until recent times, possibly due to the continuous accretion of gas that kept their star formation rate overall constant up to $z = 0$. However, lopsidedness is observed in both the young as well as the old stellar component, meaning that recent asymmetric gas accretion cannot be the only process that generates lopsidedness.

A harmonic perturbation on the order of ($m = 1$) in the mass distribution of a galactic disk produces a displacement of its center of mass, generating an internal restoring force directed toward the original center. This affects not only the density distribution but also the orbits of the particles in the disk, and it introduces kinematic asymmetries. In the plane of the disk, noncircular motions produce a radial velocity component V_R that appears as a dipolar feature (i.e., $V_R > 0$ on one side of the disk and $V_R < 0$ on the opposite side), while the tangential velocity V_Φ shows an amplitude difference between the two halves of the galaxy, with one rotation curve rising more steeply than the other (Jog 1997, 2002). For this reason, if lopsidedness arises as a result of the disk response to an external perturbation potential, the galaxy is expected to show both morphological and kinematical asymmetries (see also Jog & Combes 2009 for a review).

The combined study of stellar and gas lopsidedness in both the density and kinematics can provide important constraints on the mechanisms that trigger a lopsided perturbation. Processes such as gas accretion or ram-pressure stripping that act primarily on the gas are expected to produce a strong lopsidedness in the gas without a corresponding stellar response. Specifically, only a response in the young stellar component is expected as new stars are born from an underlying asymmetric gas distribution. However, analytical models have shown that the drag force exerted by ram-pressure stripping on the gas disk can be transmitted to the stellar disk and dark matter halo. As a result, both the stellar disk and dark matter halo can be displaced by several kiloparsecs (Smith et al. 2012). Nevertheless, the resulting distortion of the stellar disk is relatively short-lived, lasting only $\lesssim$200 Myr. Processes such as tidal interactions, however, are expected to produce a similar lopsidedness in both stars and gas since both respond to the same gravitational perturbation potential.

Previous observational studies have typically characterized lopsidedness either in the stars or gas components. In a recent work, Feng et al. (2025) studied the ionized gas velocity maps of a sample of disk galaxies from the MaNGA survey to quantify the presence of kinematic asymmetries and the correlation with global galaxy properties. They found that galaxies with large kinematic asymmetries tend to stay out of the star forming main sequence (SFMS) and below the mass-metallicity relation (MZR). Also, most asymmetric galaxies that are below the SFMS have low stellar masses (i.e., $\log_{10} M_*/M_\odot < 10.2$ within the sample), gas-phase metallicity below the MZR, and HI gas content above the stellar mass-HI relation adopted in Eq. (15) of Feng et al. (2025). For this reason, they suggest that the accretion of metal-poor gas is the main driver of the gas velocity map asymmetries in these galaxies, with the reduced star formation rate in the lower-mass systems likely associated with less efficient cooling.

In another recent work, Ghosh et al. (2025) studied the origin and evolution of a merger-induced lopsided perturbation in the stellar component of a Milky Way-like galaxy using numerical simulations. They showed that the interaction with a merging satellite galaxy produces a significant lopsided perturbation in both the stellar density and stellar velocity distributions. Furthermore, they showed that the lopsided amplitude, as well as the correlation between stellar density and stellar kinematic lopsidedness, is stronger for the metal-rich stellar component (i.e., [Fe/H] > 0) than for the metal-poor one. They argue that this is because the metal-rich stellar component has a lower velocity dispersion (i.e., kinematically colder) than the metal-poor one, and thus it is more susceptible to external perturbations. This latter result is in agreement with the finding from the previous simulation works of Varela-Lavin et al. (2023) and Fontirroig et al. (2025). Using cosmological simulations, they showed that there is a strong correlation between lopsidedness and the internal properties of the galaxies with lopsided galaxies being characterized by a lower central stellar mass density and being less gravitationally cohesive than symmetric galaxies.

Only the later work of Bilimogga et al. (2026) attempted to study the correlation between morphological and kinematical asymmetries in HI. They found that there is no straightforward correlation between morphological and kinematical asymmetries. Specifically, Bilimogga et al. (2026) studied the correlation between the asymmetry in the global HI velocity profile and in the HI spatial density, finding that a galaxy with high asymmetry in the global HI profile can have either an asymmetric HI velocity field with a symmetric HI spatial distribution or an asymmetric HI spatial distribution with an asymmetric or symmetric HI velocity field. Furthermore, they noted that an asymmetry in the HI spatial density is not necessarily associated with an asymmetry in the stellar density based on the visual inspection of the optical images, which is consistent with the lack of correlation between stellar and gas morphological lopsidedness found by Łokas (2022) in the IllustrisTNG simulations. Although a detailed quantification of the stellar asymmetry was not performed in Bilimogga et al. (2026), their results indicate that different lopsidedness triggering mechanisms might be at play to produce different levels of morphological and kinematical asymmetries in the stellar and gas components. These results are also

broadly consistent with Manuwal et al. (2022), who found multiple physical drivers contributing to HI line asymmetries in galaxies from the EAGLE simulations.

A study investigating the correlation between the stellar and gas lopsidedness both in the density and velocity distributions is still lacking. In this work, we carry out such a study using the sample of Milky Way-type galaxies from the novel Auriga Superstars simulations (Grand et al. 2017; Pakmor et al. 2025b). The high stellar mass resolution (i.e., $m_{\rm star} = 800\,{\rm M}_\odot$) of these simulations allowed us to resolve the stellar disk structure with unprecedented detail and to study its evolution in a full cosmological context by investigating the effects of different dynamical processes (e.g., tidal interactions and/or gas accretion) on the properties of galactic disks.

The paper is structured as follows. In Sect. 2 we describe the simulations from the Auriga project, the implementation of the Superstars method as described in Pakmor et al. (2025b), and the resulting Superstars galaxy sample. In Sect. 3 we characterize the lopsidedness of the stellar and HI gas disks at $z = 0$ and study the correlation between morphological and kinematical asymmetries in both the stellar and HI gas components. In Sect. 4 we investigate the evolution of lopsidedness and identify the dominant physical mechanisms driving the detected morphological and kinematical asymmetries in the stellar and HI gas components of our galaxies. Finally, in Sect. 5 we provide a summary of the results and our conclusions.

2. The data

2.1. The Auriga project

The original Auriga project consists of a suite of cosmological gravo-magnetohydrodynamical zoom-in simulations run with the moving-mesh code AREPO (Springel 2010). These halos were selected from a dark-matter-only counterpart of the Eagle simulations at $z = 0$ to be relatively isolated and have halo mass between $0.5\times10^{10} < {\rm M}_{200}/{\rm M}_\odot < 2\times10^{12}$. This halo mass range thus includes 26 dwarf galaxies (i.e., $0.5 \times 10^{10} < {\rm M}_{200}/{\rm M}_\odot < 5 \times 10^{11}$) and 30 Milky Way-type galaxies (i.e., $0.5 \times 10^{12} < {\rm M}_{200}/{\rm M}_\odot < 2 \times 10^{12}$).

The Auriga halos have been simulated at different resolutions. The original Auriga simulations trace the evolution of all halos from redshift $z = 127$ out to $z = 0$, with a mass resolution of $m_{\rm DM} = 3 \times 10^5\,{\rm M}_\odot$ for dark matter and $m_{\rm star/gas} = 5 \times 10^4\,{\rm M}_\odot$ for star particles and gas cells. The softening length of the stellar and dark matter particles evolves with time up to $z = 1$ and corresponds to a comoving softening length of 750 cpc, while the maximum physical softening length at $z < 1$ is set to 375 pc. For the gas cells, the physical softening length is scaled by the radius of the gas cell, with a minimum limit set to a value of 375 pc as for the stellar particles.

The Auriga simulations include models for primordial and metal-line cooling, for the multiphase interstellar medium, stochastic star formation and stellar evolution, for stellar feedback, as well as for the seeding and growth of supermassive black holes and feedback from active galactic nuclei, and for magnetic fields. The simulations assume a Λ cold dark matter model with the following cosmological parameters taken from Planck Collaboration XVI (2014): Hubble constant $H_0 = 67.77\,{\rm km s^{-1} Mpc^{-1}}$, matter density $\Omega_{\rm m} = 0.307$, baryonic mass density $\Omega_{\rm b} = 0.048$, and dark energy density $\Omega_\Lambda = 0.693$ (Grand et al. 2017, 2024).

A detailed description of the Auriga simulations is given in Grand et al. (2017). These simulations are now publicly available[1], and a detailed description of the data is provided in Grand et al. (2024). Throughout the paper, we refer to this particular version of the Auriga simulations as L4.

2.2. Auriga Superstars

The Auriga Superstars simulations (Superstars, hereafter) consist of nine Milky Way-type halos re-simulated with an improved stellar and dark matter particle mass resolution. The mass resolution of the gas cells is kept at the original L4 resolution (i.e., $m_{\rm gas} = 5 \times 10^4\,{\rm M}_\odot$), because the galaxy formation model implemented in Auriga was calibrated at this resolution. Within the Superstars simulations, the dark matter particle mass resolution is $m_{\rm DM} = 5 \times 10^4\,{\rm M}_\odot$ (i.e., a factor of eight better than that at the original L4 resolution), while the stellar particle mass resolution is $m_{\rm star} = 8 \times 10^2\,{\rm M}_\odot$ (i.e., a factor of 64 better than that at the original L4 resolution and than the gas cell resolution).

The increased dark matter particle mass resolution is set at the beginning of the simulation when the initial conditions are created. On the other hand, the increased stellar particle mass resolution relative to the gas cell resolution is obtained according to the following method. When a gas cell is converted into a stellar particle, 64 stellar particles are created rather than just one. The total mass of the gas cell is then divided equally among the stellar particles that were created. As a result, the mass of the resulting star particles is significantly lower than that of the gas. The newly formed stellar particles inherit the velocity of the parent gas cell plus an additional "kick" velocity term, so they evolve following different trajectories. The requirement is that this additional velocity is high enough that the stellar particles born from the same gas cell are not bound together but low enough that the properties of the galaxies do not change. The value of the "kick" velocity is unique to each stellar particle and is randomly drawn from a normal distribution with mean zero. The standard deviation is set to the minimum between the local velocity dispersion, computed from the parent gas cell and its direct neighbors, and the local sound speed. A detailed description and implementation of the Superstars method is given in Pakmor et al. (2025b).

The implementation of the Superstars method improves the visibility of substructures and features in both the stellar disk and halo, without significantly changing the global properties of the galaxies. Pakmor et al. (2025b) studied several properties of the galactic disks, such as the stellar mass surface density, the velocity dispersion, the optical radius and the disk scale height, and found that differences between the Superstars and L4 models are small and within the range of expected variability between the models due to random noise (Pakmor et al. 2025b,a). Similarly, several global properties of the galaxies, such as the halo and stellar mass and the star formation rate, are also converged between the Superstars and L4 models (Pakmor et al. 2025b). In addition to the improved mass resolution, Superstars includes high-cadence outputs of the positions and velocities of the stellar particles every 5 Myr.

The improved stellar mass resolution of Superstars allows the faint features in the stellar disk outskirts and halo to be resolved, reducing the effect of noise on the measurement of lopsidedness. In fact, in Appendix B, we see that the lower resolution lopsided profiles from the original Auriga simulations are generally noisier at larger radii than the Superstars lopsided profiles. Furthermore, the better sampling of the gravitational poten-

[1] https://wwwmpa.mpa-garching.mpg.de/auriga/index.html.

tial and the high-cadence outputs make Superstars the ideal simulation to study how different dynamical processes can affect the properties and evolution of galactic disks with unprecedented details in a fully cosmological context. In this work, we analyze a pre-final production run of the nine Milky Way-type halos modeled with the Superstars method, where an about twice times larger than intended value of the "kick" velocity was used. However, as shown in Fig. A1 of Pakmor et al. (2025b), this change in the "kick" velocity does not significantly affect the galaxies' star formation histories, nor the stellar surface density and vertical velocity dispersion within the disk optical radius. For this reason, we do not expect our results to be significantly affected by the different value of the "kick" velocity used.

2.3. The galaxy sample

2.3.1. Characterization of the stellar disks

In this work, we analyze the nine available models in Superstars. This includes galaxies with disk-to-total mass ratio (D/T), ranging from $0.35 < \mathrm{D/T} < 0.7$. Here, disk fractions are calculated considering all star particles with circularity $\epsilon > 0.7$ (see Grand et al. 2017).

Similarly to Varela-Lavin et al. (2023) and Dolfi et al. (2023), for each galaxy, we define the extension of its stellar disk at $z = 0$ as the radius, $R_{\rm opt}$, where the V-band surface brightness profile drops to 26.5 mag/arcsec^2. We also define the disk height, h_{90}, as the distance above and below the galactic plane enclosing 90% of the total stellar mass located within a projected radius of $1\,R_{\rm opt}$. The measurement of both $R_{\rm opt}$ and h_{90} is performed after rotating each galaxy to a face-on orientation. To do this, we center the galaxy on the position of its most bound particle and calculate its total stellar angular momentum using only the young stellar particles ($\leq$1 Gyr old) contained within a sphere of radius $0.2\,R_{200}$, where R_{200} is the radius within which the mean enclosed density is 200 times the critical density of the Universe (hereafter, the "virial radius"). We then align it with the z-axis of a Cartesian coordinate system. In this way, the face-on disk corresponds to the xy projection, while the edge-on disk corresponds to the xz and yz projections.

2.3.2. Characterization of the HI gas disks

For each galaxy, we also calculated the atomic hydrogen (i.e., HI) mass fraction of each individual gas cell. To do this, we followed the approach described in detail in Sect. 3 of Marinacci et al. (2017), where the HI gas cell mass is expressed as

$$\mathrm{M_{HI},}_i = (1 - f_{\mathrm{mol},i}) f_{\mathrm{neutr},i} X_{\mathrm{H},i} \mathrm{M_{gas},}_i, \tag{1}$$

where $f_{\mathrm{mol},i}$ and $f_{\mathrm{neutr},i}$ are the molecular and neutral hydrogen gas mass fractions, respectively, $X_{\mathrm{H},i}$ is the hydrogen mass fraction; and $\mathrm{M_{gas},}_i$ is the total gas mass of the individual gas cell.

The evolution of the hydrogen fraction, $X_{\mathrm{H},i}$, and gas cell mass, $\mathrm{M_{gas},}_i$, is directly tracked within `AREPO` and the Auriga galaxy formation model; therefore, both quantities are available from the simulation output. The neutral hydrogen fraction, $f_{\mathrm{neutr},i}$, is calculated from the gas cooling module, implemented within Auriga, for each individual gas cell by modeling an ionization network for hydrogen and helium that includes processes such as collisional ionization, collisional excitation, recombination, free-free emission, and Compton cooling (Ikeuchi & Ostriker 1986; Katz et al. 1992, 1996) in the presence of a time-varying photo-ionizing UV background (Faucher-Giguère et al. 2009). A detailed description of the gas cooling implementation within the Auriga galaxy formation model is provided in Vogelsberger et al. (2013). In our analysis, we use this value of the neutral hydrogen fraction, $f_{\mathrm{neutr},i}$, calculated directly from the gas cooling module and stored for each gas cell in the Auriga simulation output.

Then, we determined the molecular hydrogen fraction, $f_{\mathrm{mol},i}$, using the empirical relation from Blitz & Rosolowsky (2006), where the ratio between the molecular and atomic hydrogen volumetric densities (i.e., $R_{\rm mol}$) is defined as

$$R_{\mathrm{mol},i} = \left(\frac{P}{P_0}\right)^{\alpha}, \text{with } P = [(\gamma - 1)\rho]u, \tag{2}$$

with P the gas pressure of each gas cell defined by the effective equation of state, ρ the mass density of the gas cell and u its thermal energy per unit mass (Springel & Hernquist 2003). $P_0 = 1.7 \times 10^4\,\mathrm{Kcm^{-3}}$ and $\alpha = 0.8$ are free parameters that we fix to the values determined by Leroy et al. (2008) based on a set of observations of nearby galaxies. The fraction of the molecular hydrogen is then calculated as

$$f_{\mathrm{mol},i} = \frac{R_{\mathrm{mol},i}}{(R_{\mathrm{mol},i} + 1)}. \tag{3}$$

Finally, we computed the HI gas mass as described in Eq. (1).

In Fig. 1, we show the face-on projection of the present-day V-band stellar surface brightness maps (left panels) and of the HI surface density maps (right panels) of the nine Superstars galaxies. The galaxy labels used here are the same as they were defined in the original Auriga simulations by Grand et al. (2017). The dashed and solid orange circles define the outer disk region between 0.5 and $1\,R_{\rm opt}$, respectively, measured from the stellar surface brightness profiles, as described at the beginning of the section. The extent of each image, centered on the galaxy, ranges from $-2\,R_{\rm opt}$ to $+2\,R_{\rm opt}$ along both axes. We see that all galaxies show a disk morphology, extending out to $\sim 1\,R_{\rm opt}$, in both stellar and HI components. Only Au22 shows a compact stellar disk, as well as the lowest HI surface density and the least extended HI spatial distribution, while Au25 shows signs of a perturbed stellar and HI disk. Some galaxies (i.e., Au17, Au18, and Au22) also show a very strong stellar bar in the inner regions within $0.5\,R_{\rm opt}$. In Table 1, we summarize the main properties at $z = 0$ of the nine Superstars galaxies studied in this work, along with their values of the present-day global morphological and kinematical lopsidedness for both stars and HI gas measured as described in the following Sects. 3.1 and 3.2.

3. The present-day stellar and HI gas lopsidedness

As described in detail in the introduction (see Sect. 1), distinct dynamical processes can trigger different responses in the stellar and gas components. In this section we study the correlation between stellar and HI gas lopsidedness in both density and kinematics for the nine Superstars galaxies, focusing on $z = 0$. We highlight here that, when studying global galaxy properties, we use both Superstars and the original L4 Auriga galaxies (see Sects. 3.3.1, 3.3.2, and 3.4.1) to increase the sample statistics. Specifically, we include in our sample nine L4 galaxies with disk-to-total ratio $\mathrm{D/T} \geq 0.5$ at $z = 0$. In Table A.1, we summarize the main properties at $z = 0$ of these nine L4 galaxies, along with their values of the present-day global morphological and kinematical lopsidedness for both stars and HI gas. However, when analyzing density and velocity maps (see Sects. 2.3 and 3.4) and the lopsidedness time evolution (see Sect. 4), we

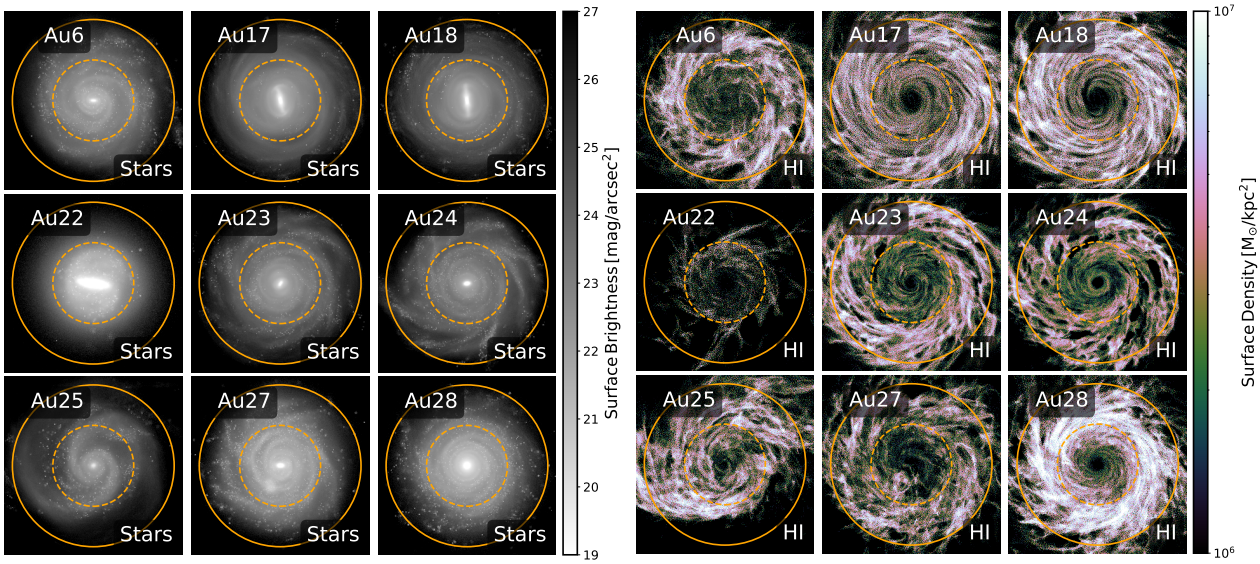


Fig. 1. *Left panels*: Present-day face-on V-band stellar surface brightness maps of the nine galaxies in Superstars. The dashed and solid orange circles define the region at 0.5 and 1 $R_{\rm opt}$, respectively, where $R_{\rm opt}$ has been calculated as described in Sect. 2.3.1. The extent of each image, centered on the galaxy, ranges from $-2\,R_{\rm opt}$ to $+2\,R_{\rm opt}$ along both axes (see Table 1 for the $R_{\rm opt}$ value of each galaxy). *Right panels*: Same but showing the present-day face-on HI surface density maps. It is worth noting the presence of a satellite galaxy within $0.5\,R_{\rm opt}$ in Au27, which suggests that this galaxy is undergoing an interaction.

Table 1. Properties of Superstars galaxies.

ID	M_* (10^{10} M$_\odot$)	$M_{\rm HI}$ (10^{10} M$_\odot$)	$R_{\rm opt}$ (kpc)	M_{200} (10^{12} M$_\odot$)	$\langle A_1 \rangle$ (Stars – HI)	$\langle A_{1,\rm kin} \rangle$ (Stars – HI)
Au6	5.76	1.10	26.5	1.02	0.11 – 0.12	0.12 – 0.38
Au17	7.94	1.46	27.4	1.13	0.08 – 0.09	0.08 – 0.30
Au18	7.23	1.57	27.4	1.14	0.03 – 0.06	0.03 – 0.37
Au22	7.67	0.17	17.7	0.99	0.05 – 0.18	0.03 – 0.29
Au23	8.97	1.97	35.3	1.51	0.09 – 0.11	0.05 – 0.38
Au24	8.05	1.56	36.2	1.51	0.06 – 0.09	0.03 – 0.32
Au25	3.80	2.14	30.2	1.22	0.27 – 0.24	0.21 – 0.41
Au27	10.13	1.22	28.8	1.74	0.07 – 0.07	0.10 – 0.39
Au28	10.95	1.84	27.4	1.58	0.06 – 0.06	0.02 – 0.32

Notes. Main properties of the nine Superstars galaxies at $z = 0$. From the left to the right column: galaxy ID, total galaxy stellar mass (M_*), total galaxy HI gas mass ($M_{\rm HI}$), stellar optical radius in the V band ($R_{\rm opt}$), halo mass (M_{200}), galaxy global morphological lopsidedness for both stars and HI gas ($\langle A_1 \rangle$), and global galaxy kinematical lopsidedness for the stars and HI gas ($\langle A_{1,\rm kin} \rangle$).

use only the Superstars galaxies due to their higher mass and temporal resolutions.

3.1. Measuring morphological lopsidedness

Following the previous works of Varela-Lavin et al. (2023) and Dolfi et al. (2023, 2025), we calculate the morphological lopsidedness by measuring the amplitude of the first Fourier mode, $m = 1$, from the galaxy stellar or gas mass distribution in concentric radial annuli and normalizing it by the zeroth mode, $m = 0$, after rotating the galaxy to a face-on orientation, as described in Sect. 2.3.1. The amplitude of the mth Fourier mode in a given radial annulus is defined as

$$A_m(R_j) = \sqrt{a_m(R_j)^2 + b_m(R_j)^2}, \tag{4}$$

where $a_m(R_j)$ and $b_m(R_j)$ are defined as

$$a_m(R_j) = \sum_i \mathrm{M}_i \cos(m\theta_i)$$
$$b_m(R_j) = \sum_i \mathrm{M}_i \sin(m\theta_i). \tag{5}$$

In Eq. (5), M_i and θ_i represent the mass and azimuthal angle of the ith stellar particle within a given radial annulus, respectively. The morphological lopsidedness is finally quantified in each radial annulus as

$$\mathrm{A}_1(R_j) = \frac{A_1(R_j)}{A_0(R_j)}. \tag{6}$$

We defined equally spaced concentric radial annuli with a width of 0.5 kpc and a height of $2|h_{90}|$ from the galactic plane, extending from the center of the galaxy out to $1\,R_{\rm opt}$. Finally, to quantify the global morphological lopsidedness of the galaxy ($\langle A_1 \rangle$, hereafter), we calculated the average $\mathrm{A}_1(R_j)$ in the radial range between 0.5–1 $R_{\rm opt}$. Galaxies with $\langle A_1 \rangle > 0.1$ are classified as lopsided, while those with $\langle A_1 \rangle < 0.1$ are considered symmetric. The value $\langle A_1 \rangle = 0.1$ is typically used in observations as the threshold separating lopsided and symmetric galaxies (Bournaud et al. 2005).

3.2. Measuring kinematical lopsidedness

As described in the introduction (Sect. 1) a tidally induced lopsided perturbation is expected to show both morphological and kinematical asymmetries. Therefore, by quantifying the kinematical lopsidedness and studying its correlation with the morphological counterpart, we aim to verify whether this is the case and to constrain the mechanisms responsible for triggering mechanisms.

To quantify the kinematical lopsidedness in the stellar and HI gas component of our galaxy sample, we decomposed the velocity of each particle into its components using cylindrical

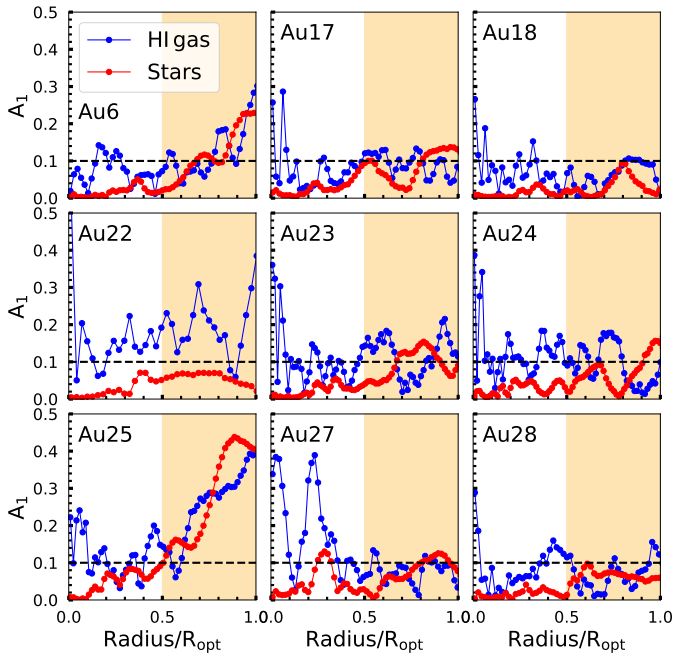


Fig. 2. Present-day morphological lopsided profiles of the stellar and HI mass distributions within the galactic disks of the nine galaxies in Superstars. The shaded orange region marks the radial interval between 0.5–1 R_{opt} used to quantify the global lopsidedness of the galaxy. The horizontal dashed line represents the lopsidedness threshold $\langle A_1 \rangle = 0.1$.

coordinates, namely tangential V_Φ, radial V_R, and vertical V_z, after rotating the galaxy to a face-on orientation. In this work, we focus on the radial component of the velocity, V_R. Similar to the morphological lopsidedness, we calculated the kinematical lopsidedness by measuring the amplitude of the first Fourier mode from the galaxy radial velocity, normalized by the zeroth mode (see Eqs. 4–6). We used the same concentric radial annuli defined in Sect. 3.1. Finally, the global kinematical lopsidedness of the galaxy ($\langle A_{1,kin} \rangle$ hereafter) was calculated as the average $A_1(R_j)_{kin}$ in the radial range between 0.5-1 R_{opt}, as for the morphological lopsidedness. For the kinematical lopsidedness, we adopted the same threshold, $\langle A_{1,kin} \rangle = 0.1$, as used for the morphological lopsidedness to distinguish between lopsided and symmetric galaxies, as described in Sect. 3.1. We note here that we measured the morphological (see Sect. 3.1) and kinematical lopsidedness of both the stellar and HI gas components over the same spatial region, which is defined by the extension of the stellar disk reaching out to 1 R_{opt} and with a vertical extent of $2|h_{90}|$ from the galactic plane, calculated as described in Sect. 2.3.1.

3.3. Superstars: The present-day A_1 density profiles

In Fig. 2, we show the present-day A_1 profiles of the stellar and HI gas mass distributions within the galactic disk for the Superstars galaxies, calculated as described in Sect. 3.1. We observed that while the HI gas shows greater fluctuations in its profiles than the stars, there is an overall good agreement between the profiles of the two tracers. Specifically, the two lopsided galaxies (i.e., Au6 and Au25) that show increasing stellar A_1 profiles when moving to the disk outskirts also show increasing A_1 profiles when considering the HI density distribution. On the other hand, galaxies with symmetric stellar distribution also typically show symmetric HI distributions. The only exception is Au22, which shows a discrepancy between the stellar and HI A_1 profiles, suggesting a specific driving mechanism for the lopsidedness that affects only the gas distribution.

We also see that, while the stars do not show any significant lopsidedness in the inner galactic regions within 0.5 R_{opt}, the HI gas lopsided amplitude shows peaks in almost all of the galaxies. These strong and localized lopsided features, confined to the inner galactic regions and appearing only in the HI gas, could arise from a combination of effects. First, they may be partly driven by the low HI gas mass surface density within the inner ∼2–3 kpc. As shown in Fig. 1, the HI gas distribution exhibits a central depression, a feature often observed in galaxies due to the increasing molecular gas fraction toward their centers. As a result, the measurement of lopsidedness in the central regions is based on relatively little HI gas, making it more susceptible to small fluctuations and asymmetries that can lead to artificially large values of the lopsided amplitude. In addition, bar-driven gas asymmetries may also contribute in the case of those galaxies where we see a strong stellar bar in the central regions (e.g., Au17, Au18, and Au22; see Fig. 1. As described in Fragkoudi et al. (2025), the bar strength is quantified by measuring the amplitude of the $m = 2$ Fourier mode of the galaxy stellar mass distribution, normalized by the $m = 0$ mode, and taking its maximum value within the inner 10 kpc (see also Eqs. 4–6). The bar strength typically peaks within 5 kpc, providing an approximate estimate of the region where the bar dominates. This roughly corresponds to the radial range where we observe peaks in the HI gas lopsided amplitude. Therefore, the bar may be driving these gas asymmetries. Finally, strong Active Galactic Nuclei (AGN) activity as in the case of Au22 (Grand et al. 2017) may also contribute to these central HI asymmetries. On the contrary, in the case of Au27, the presence of a satellite galaxy within 0.5 R_{opt} may be responsible for both the central gas and stellar asymmetries seen in Fig. 2.

We note that, in this work, we study the lopsidedness of the stellar and HI gas over the same spatial region, defined by the stellar R_{opt} calculated as described in Sect. 2.3.1. However, observational studies have shown that HI disks can be 2–3 times more extended than the optical stellar disk (Bosma 1981) and frequently exhibit lopsided asymmetries in the outer galactic regions (Bournaud et al. 2005; Jog & Combes 2009). We therefore inspected the HI lopsided profiles beyond the stellar R_{opt}, out to R^{95}_{HI}, defined as the radius enclosing 95% of the total HI gas mass. Although these results are not shown in the paper, we find that eight out of nine of the galaxies exhibit lopsided HI distributions in the outer regions out to R^{95}_{HI}.

3.3.1. The stellar-HI density lopsidedness correlation

In Fig. 3, we show the present-day $\langle A_1 \rangle$ of the stellar and HI gas disks for the Superstars galaxies. We also include here the nine L4 disk galaxies with D/T > 0.5 that are not modeled with Superstars, as mentioned in Sect. 3. In fact, as shown in Appendix B, we find that lopsidedness is well converged with stellar mass resolution. Therefore, the inclusion of the original L4 galaxies is unlikely to affect our correlation results when studying global galaxy properties. Galaxies are color coded by their central stellar mass density, μ_*, defined in Appendix B. The diagonal dashed black line indicates the one-to-one relation between the stellar and HI gas asymmetry.

We found a strong correlation between the $\langle A_1 \rangle$ in the stars and HI gas disks (i.e., galaxies with large lopsidedness in the stars have also typically large lopsidedness in the HI gas, and vice-versa), suggesting that the two tracers are dynamically

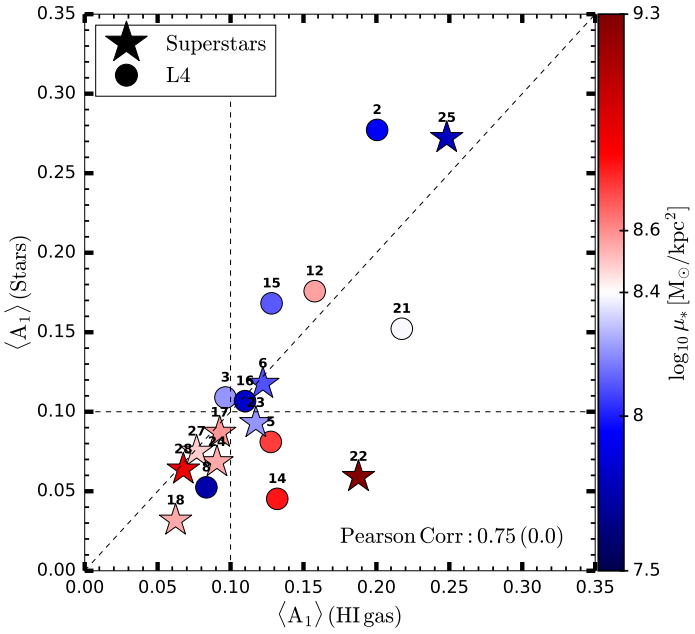


Fig. 3. Present-day global lopsidedness of the stellar and HI disks of the nine galaxies in Superstars. We also include nine additional L4 disk galaxies with D/T > 0.5 that are not modeled in Superstars (circle symbols). The value of the Pearson correlation coefficient is reported in the figure, with the p-value indicated within brackets. Markers are color coded by the central stellar mass density μ_* of each galaxy, calculated as described in Sect. 3.3.1. The global lopsidedness has been measured as described in Sect. 3.1. The diagonal dashed line indicates the one-to-one relation, while the vertical and horizontal dashed lines represent the lopsidedness threshold $\langle A_1 \rangle = 0.1$.

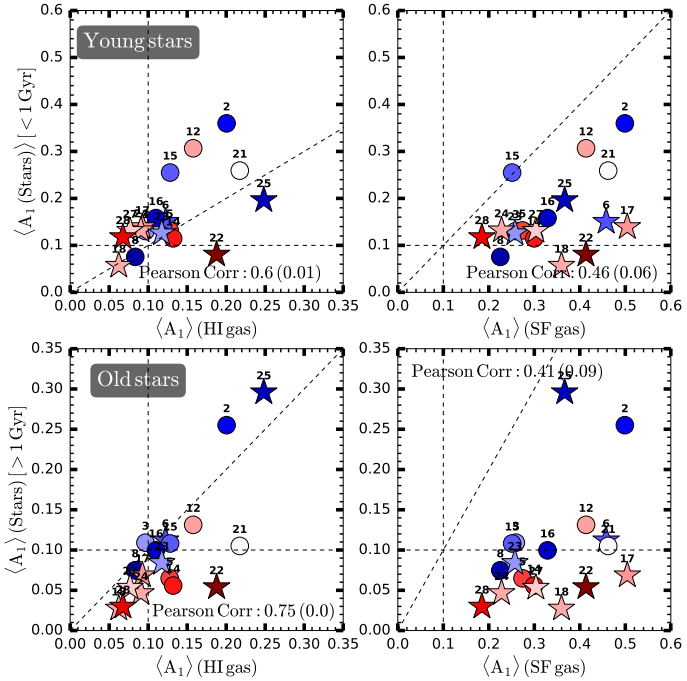


Fig. 4. *Top panels*: Present-day global lopsidedness of the young stellar component (< 0.5 Gyr old) compared with that of the HI (*left*) and star-forming (*right*) gas components. *Bottom panel*: Same but for the old stellar component (>0.5 Gyr old). The symbols have the same meaning as in Fig. 3.

coupled. The strong positive linear correlation between stellar and HI gas lopsidedness is also supported by the high value of the Pearson coefficient reported in Fig. 3. Furthermore, we see that the two most strongly lopsided galaxies (i.e., Au2 and Au25) are among those with the lowest central stellar mass density and that, although there are clear exceptions, the central stellar mass density tends to increase as we move along the diagonal line toward the most symmetric galaxies. This is consistent with the strong anticorrelation found between lopsided amplitude and central stellar mass density in both observations (Reichard et al. 2008) and simulations (Fontirroig et al. 2025). Therefore, as two-thirds of the Superstars galaxies have central stellar mass densities (μ_*) above the sample average, this explains our moderate bias toward symmetry at the present day. In Fig. 3, we see that there are three galaxies from the original L4 simulations (i.e., Au8, Au12, and Au21), which represent an exception to the anticorrelation observed between lopsided amplitude and central stellar mass density. Two of these galaxies (i.e., Au12 and Au21) have high $\langle A_1 \rangle$ in both stars and HI gas, and relatively high central stellar mass density. These galaxies have experienced a significant recent interaction (< 5 Gyr ago) with a satellite of total mass $\gtrsim 10^{10}\,M_\odot$, as also shown by Gómez et al. (2017), which likely triggered their lopsidedness and produced the observed misalignment between the inner disk and the outer shells of the dark matter halo (see figure 8 of Gómez et al. 2017). On the other hand, Au8 has one of the lowest central stellar mass density, but also a low $\langle A_1 \rangle$ in both stars and HI gas. Visual inspection of the evolutionary history of this galaxy reveals that it is currently experiencing an interaction with a satellite. However, the pericentric passage of this satellite primarily triggered a symmetric two-armed spiral ($m = 2$) pattern in both the stellar and HI gas density distributions, rather than inducing a lopsided ($m = 1$) asymmetry. Finally, another exception in Fig. 3 is Au22, which is characterized by the highest central stellar mass density and shows high $\langle A_1 \rangle$ only in the HI gas. As already mentioned in Sect. 3.3, this might suggest a particular driving mechanism for the lopsidedness that primarily affects the gas distribution without a corresponding stellar response, as well as the lack of a significant massive interaction capable of perturbing the compact stellar disk of this galaxy. We explore the triggering mechanisms of lopsidedness in the Superstars galaxies further in Sect. 4.

In the left panels of Fig. 4, we separately show the correlation between $\langle A_1 \rangle$ of young (<0.5 Gyr old; top panels) and intermediate+old-age (>0.5 Gyr old; bottom panel)[2] stars and that of the HI gas. We choose an age cut of <0.5 Gyr old for the young stars in order to trace recent star formation. In the bottom-left panel, a strong positive correlation between the stellar and HI gas lopsidedness persists even after removing the youngest stars, as also supported by the high Pearson coefficient. This indicates that the old stellar component is dynamically coupled to the HI gas and traces asymmetries in the overall mass distribution of galaxies. The correlation between the lopsided amplitude of the old stellar component and the star-forming gas is weaker likely because older stars have had sufficient time to phase-mix (see bottom-right panel of Fig. 4). On the other hand, in the top panels, we see that the correlation between the young stellar and HI gas lopsidedness is less strong, with the young stars typically showing higher $\langle A_1 \rangle$ amplitude than the HI gas. This is due to the fact that lopsidedness in the young stars is more closely related to asymmetries in the star-forming gas (see top-right panel of Fig. 4). This means that strong lopsidedness in the young stars

[2] Hereafter, referred to as "old stars" for simplicity.

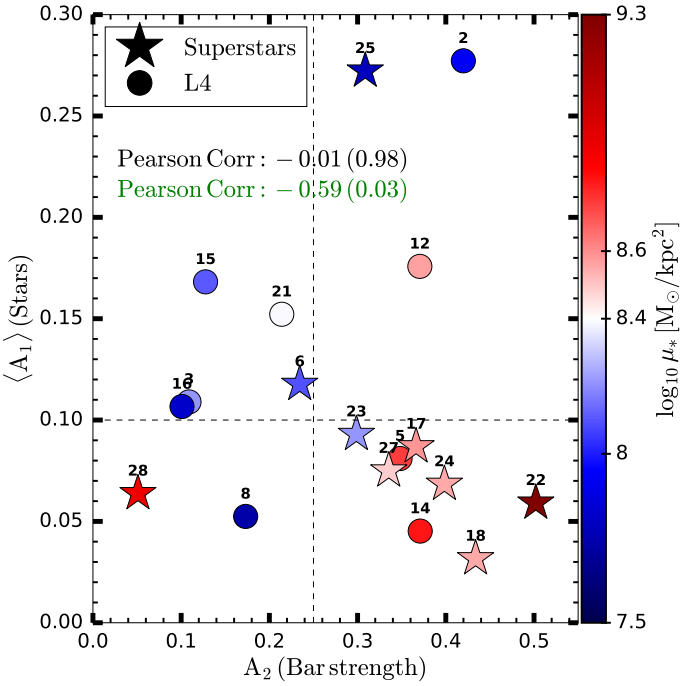


Fig. 5. Correlation between the present-day global lopsidedness of the outer stellar disk and the present-day central bar strength of the nine Superstars and nine L4 galaxies. Two values of the Pearson coefficient are reported. The top one was obtained considering all the galaxies, while the bottom one excludes four outliers (i.e., Au2, Au8, Au25, and Au28). The symbols have the same meaning as in Fig. 3. Markers are color coded by the central stellar mass density (μ_*) of each galaxy, calculated as described in Sect. 3.3.1. The bar strength has been measured as described in Sect. 3.3.2, following Fragkoudi et al. (2025). The horizontal dashed line indicates the lopsidedness threshold $\langle A_1 \rangle = 0.1$, while the vertical dashed line at $A_2 \geq 0.25$ represents the threshold used in Fragkoudi et al. (2025) to classify barred and unbarred galaxies.

(and not in the old stellar component) is an indicator of asymmetric star formation.

The results presented in Fig. 3 and 4 appear to contrast with those from Łokas (2022), who did not find any clear correlation between the stellar and gas lopsidedness in their sample of disk galaxies selected from the IllustrisTNG (TNG100) simulations (see figure 10 in Łokas 2022). However, several factors may account for these differences. First, Łokas (2022) studied the lopsided distribution of the total gas component, whereas we focus specifically on neutral hydrogen. Second, Łokas (2022) measured the global lopsidedness of both stars and gas within 1–2 R_h, where R_h is the half-mass radius of the galaxy, while we quantify lopsidedness in the outskirts of the galactic disk between 0.5–1 R_{opt}. The different radial intervals used to measure lopsidedness are likely to affect its strength (see also Dolfi et al. 2023), particularly for the gas component, which is typically more extended than the stellar disk. Finally, Łokas (2022) analyzed lopsidedness in the TNG100 simulation, which has a mass resolution of $m_{DM} = 7.5 \times 10^6\,M_\odot$ for dark matter and $m_{gas} = 1.4 \times 10^6\,M_\odot$ for gas (Nelson et al. 2019). This is approximately one and two orders of magnitude lower than the dark matter and gas mass resolution of the original Auriga simulation, respectively (see Sect. 2.1). The relatively low resolution of the TNG100 simulation, with respect to the models analyzed in this work, is likely to influence the development of perturbations producing lopsidedness, thereby affecting its onset, strength, and lifetime.

3.3.2. The stellar density lopsidedness-bar connection

Previous works that studied the presence of morphological features in disk galaxies, such as stellar bars and lopsidedness, have shown that strong lopsidedness is more easily induced in galaxies that have low central stellar mass density and are less gravitationally cohesive (Reichard et al. 2008; Varela-Lavin et al. 2023). Furthermore, lopsided galaxies are also found to have assembled their stellar mass, on average, at later times than symmetric galaxies (Dolfi et al. 2023). On the contrary, barred galaxies are typically found to be more baryon-dominated and to have assembled their stellar mass at early times (Fragkoudi et al. 2025). This means that galaxies that are prone to develop a stellar bar should be less likely to develop a lopsided perturbation based on their internal properties.

In Fig. 5, we show the correlation between the stellar $\langle A_1 \rangle$ and the bar strength at $z = 0$ for the Superstars galaxies, as well as for the nine L4 disk galaxies with D/T > 0.5 that are not modeled with Superstars. We quantify the bar strength ($\langle A_2 \rangle$ hereafter) as described in Sect. 3.3, by taking the maximum value of the $m = 2$ Fourier mode in the inner 10 kpc calculated following Eqs. (4)–(6). We find an anticorrelation between the stellar density lopsidedness in the outer galactic disk and the bar strength in the inner galactic regions (i.e., galaxies with high $\langle A_1 \rangle$ tend to have low $\langle A_2 \rangle$, and vice versa), although clear exceptions exist. When considering the full galaxy sample, the Pearson coefficient indicates no significant correlation (top value in Fig. 5). However, after removing the clear outliers (i.e., Au2, Au8, Au12, Au25, and Au28), we find a moderate anticorrelation (bottom value in Fig. 5). Additionally, we see that the most strongly barred galaxies tend to have high central stellar mass density, whereas the lopsided galaxies are typically characterized by low central stellar mass density. These results suggest that the anticorrelation between lopsidedness and bar strength shown in Fig. 5 is a result of the strong correlation of both quantities with the galaxy central stellar mass density. In particular, galaxies with higher central stellar mass density tend to be less susceptible to developing lopsided perturbations while being more likely to host strong bars. These conclusions are further supported by the results of Fontirroig et al. (2025), who trained a supervised random forest algorithm on a sample of ∼8000 galaxies from the TNG50 simulations. They found that the algorithm could successfully distinguish between lopsided and symmetric galaxies (with an ∼80% accuracy) using only their internal properties, with the galaxy central stellar mass density being the most important feature for the classification.

Regarding the outliers in the anticorrelation between stellar density lopsidedness and bar strength mentioned above, Fragkoudi et al. (2025), who studied the bar formation in the original Auriga simulations, showed that Au2 hosts a strong bar that formed at early times ∼7 Gyr ago, while Au12 and Au25 host a bar that formed more recently at ∼2.5 and < 1 Gyr ago, respectively. All these three galaxies have also experienced a strong and recent interaction with a massive satellite (i.e., $M_{tot} > 10^{10.5}\,M_\odot$; see Gómez et al. 2017) within the last 5 Gyr. This interaction could have triggered the subsequent formation of both morphological features (i.e., stellar bar+stellar density lopsidedness) in Au12 and Au25. However, Au2 hosts an ancient bar and one of the most extended disks in the L4 simulation (Grand et al. 2017). As shown in Grand et al. (2017), the extended disk of Au2 results from a merger occurring in the plane of the disk between ∼8 and ∼7 Gyr ago. During this period, the bar also formed. This coplanar satellite accretion may therefore have triggered both the bar formation and the disk growth.

Once the disk became significantly extended (~6.5 Gyr ago) subsequent satellite interactions occurring over the last 5 Gyr could more easily perturb the outer galactic disk due to its lower self-gravity (very extended disk and low central stellar mass density), without significantly affecting the inner regions.

In a previous work, Łokas (2022) also found that lopsided stellar disks tend to have weaker bars (i.e., a low value of $\langle A_2 \rangle$) than symmetric ones from the analysis of a sample of disk galaxies from the IllustrisTNG simulations, consistent with our results. However, these results appear in disagreement with those from Bournaud et al. (2005), who found that the $m = 1$ mode is correlated with the presence of $m = 2$ features in their observational galaxy sample, where A_2 is measured as the average value over the radial range between 1.5 and 2.5 disk scalelengths (see Fig. 8 of Bournaud et al. 2005). Interestingly, they found that a similar correlation persists when measuring A_2 over the radial ranges between 0.5 and 1.5 disk scalelengths (i.e., central regions) and between 2.5 and 3.5 disk scalelengths (i.e., outer regions). They therefore concluded that the presence of $m = 2$ features is correlated with the presence of lopsidedness. However, they did not further investigate the nature of these $m = 2$ features, whether they are primarily associated with the presence of a central bar or with outer bi-symmetric structures, such as two-armed spiral patterns.

Overall, the results shown in Fig. 5 suggest that the observed anticorrelation between the presence of stellar density lopsidedness and the presence of a bar arises as a result of the internal properties of the galaxies, such as their central stellar mass distribution, which is found to be a key parameter in determining whether a galaxy is susceptible to lopsidedness or bar formation. In a follow-up work, we will investigate in more detail the origin of the anticorrelation between stellar density lopsidedness and bar strength, as well as the formation and survival of both morphological features in galaxies.

3.4. Superstars: The present-day V_R maps

In Fig. 6, we show the present-day face-on mass-weighted mean radial velocity maps of the stellar and HI gas disks for the Superstars galaxies. We see that almost all galaxies in Fig. 6 show a dipolar feature in the outer regions of the HI radial velocity maps (i.e., between 0.5–1 R_{opt}, orange circles), which is a signature of kinematical lopsidedness. On the contrary, only three galaxies show a dipolar feature in the outer regions of the stellar radial velocity maps (i.e., Au6, Au25, and Au27). Among these, two galaxies (i.e., Au6 and Au25) are also currently lopsided in both the stellar and HI gas density distributions (see Sect. 3.3), as expected if lopsidedness arises as the result of an external perturbation potential. For the remaining galaxies, which do not show dipolar features in the outer regions of the stellar radial velocity maps, the different levels of kinematic asymmetries in the stellar and HI gas disks might indicate other lopsidedness triggering mechanisms. In what follows (Sect. 3.4.1), we quantify the kinematical lopsidedness of both the stellar and HI gas disks and examine its correlation with the corresponding morphological lopsidedness, in order to investigate the different mechanisms that may trigger lopsidedness.

From the radial velocity maps in Fig. 6, we also see that many of them shows a quadrupole feature in the inner galactic regions within 0.5 R_{opt} in both the stellar and HI gas velocity maps. In particular, three galaxies (i.e., Au17, Au18, and Au22) show the strongest quadrupole signal, which is indicative of elongated orbits driven by a stellar bar.

3.4.1. Kinematic-morphological lopsidedness correlation

In Fig. 7, we show the correlation between the present-day kinematic $\langle A_{1,kin} \rangle$ and morphological $\langle A_1 \rangle$ lopsidedness of the stellar and HI gas disks for the Superstars galaxies, as well as for the L4 disk galaxies with D/T > 0.5, measured as described in Sects. 3.1 and 3.2. Galaxies are color coded by the average amplitude of the kinematic Fourier m = 2 coefficient calculated from the face-on projected radial velocity maps of both stars and HI gas in the outer regions of the galactic disk between 0.5–1 R_{opt}. A nonzero kinematic $\langle A_{2,kin} \rangle$ in the outer galaxy regions is typically associated with spiral arms.

For the stellar component, we find that kinematical and morphological lopsidedness are well correlated, indicating that stellar lopsidedness likely arises from a perturbed gravitational potential that coherently affects both stellar orbits and their spatial distribution. In contrast, for the HI gas, we find a weaker correlation between kinematical and morphological lopsidedness, with the lopsided signature being generally stronger in the kinematics than in the morphology. Previous works have associated strong gas kinematic asymmetries with gas accretion (Feng et al. 2025). However, this does not exclude the possibility that lopsidedness results from external interactions, given the strong correlation that we find between the stellar and HI gas morphological lopsidedness in Sect. 3.3.1. Therefore, the results shown in Fig. 7 suggest that, independent of whether lopsidedness is generated through tidal interactions or gas accretion, its imprint is stronger in the HI gas kinematics than in its morphology.

In a previous work, Bilimogga et al. (2026) studied the correlation between the asymmetry in the global HI velocity profiles and the HI morphological asymmetry in their observed galaxy sample. Specifically, they found that a galaxy with a strongly asymmetric HI velocity field can have either a symmetric or asymmetric HI density distribution. In this work, we find similar results. In fact, as shown in the right-hand panel of Fig. 7, we find galaxies such as Au27 and Au28 characterized by a symmetric HI density distribution, $A_1(\mathrm{HI\,Morph}) \lesssim 0.1$, but still asymmetric HI kinematics, $A_1(\mathrm{HI\,Kinem}) > 0.1$, as well as galaxies such as Au6 and Au25 characterized by both an asymmetric HI density distribution, $A_1(\mathrm{HI\,Morph}) > 0.1$, and asymmetric HI kinematics, $A_1(\mathrm{HI\,Kinem}) > 0.1$. However, while Bilimogga et al. (2026) reported a lack of correlation between stellar and HI density lopsidedness, we find that the two are strongly correlated, as previously shown in Fig. 3. It is important to note, however, that Bilimogga et al. (2026) classified optical asymmetries based on visual inspection. Therefore, it is not specified whether stellar and HI asymmetries were measured over the same spatial extent. As discussed in Sect. 3.3.1, the different spatial regions used to quantify stellar and HI asymmetries might affect the resulting correlation, given that lopsidedness is stronger at larger radii and that HI is generally more extended than the stellar component. Alternatively, differences in the environments where the galaxies reside might also affect the correlation between stellar and HI asymmetries. In fact, while Bilimogga et al. (2026) studied HI asymmetries in galaxies located in group environments, this work focuses on galaxies in the field. Consequently, the lack of correlation between HI and stellar morphological asymmetries reported by Bilimogga et al. (2026) may also suggest that lopsidedness is triggered by mechanisms, such as ram-pressure stripping, that directly affect the gas but not the stellar component.

Our results, so far, favor a scenario in which lopsidedness is triggered by tidal interactions and/or gas accretion. In particular, we have found the following:

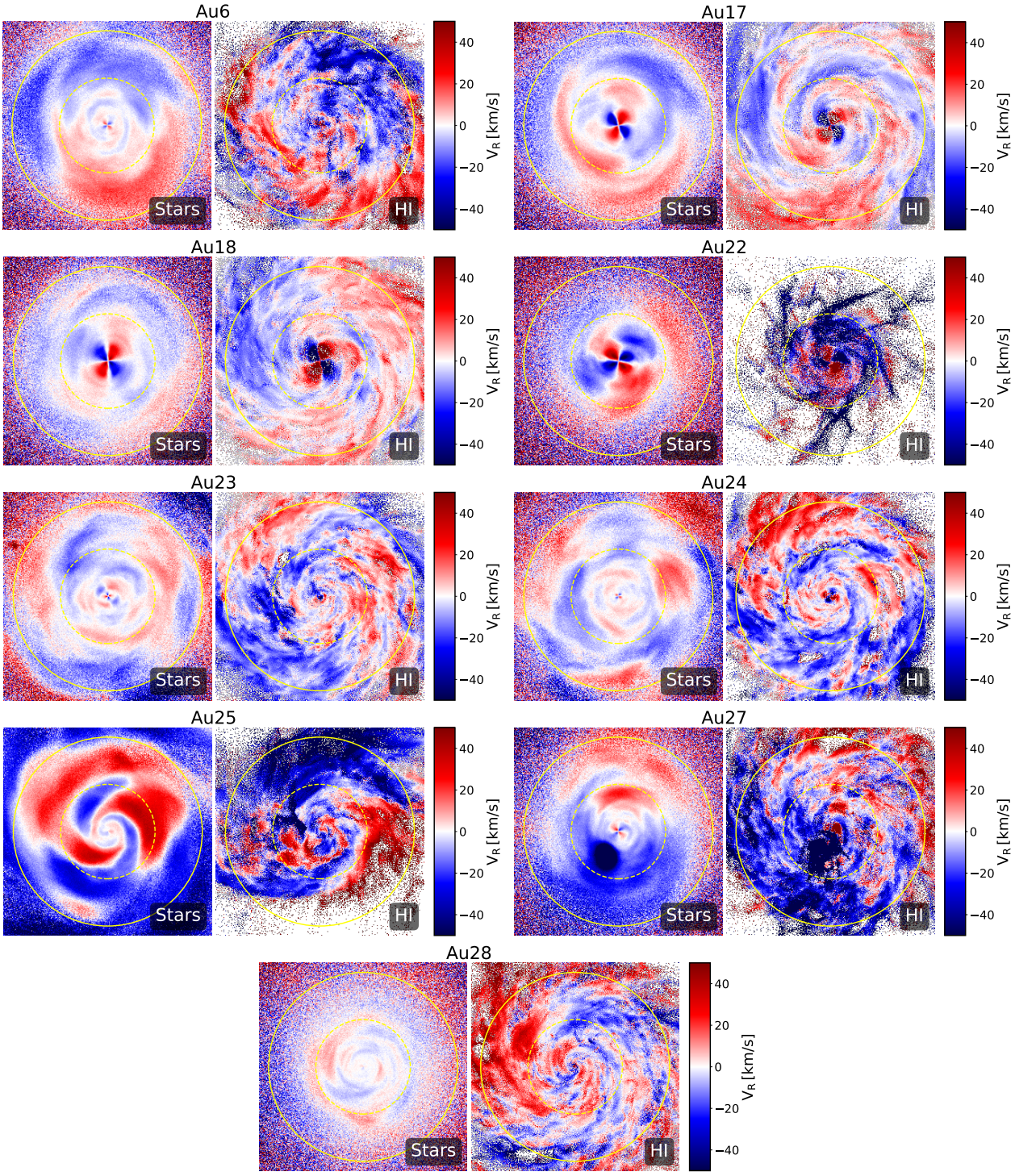


Fig. 6. Face-on projections of the present-day radial velocity maps of the stars and HI disks of the nine galaxies in Superstars. The radial velocity map of each galaxy has been obtained as described in Sect. 3.2. The dashed and solid yellow circles define the region at 0.5 and 1 R_{opt}, respectively, where R_{opt} has been calculated as described in Sect. 2.3.1.

1. A strong correlation between stellar and HI gas morphological asymmetries (see Sect. 3.3.1),
2. A strong correlation between kinematical and morphological asymmetries in the stellar component (see left-hand panel of Fig. 7), and
3. A weak correlation between kinematical and morphological asymmetries in the HI gas, which is typically characterized by stronger kinematical than morphological asymmetries (see right-hand panel of Fig. 7).

Galaxies with asymmetric HI morphology and asymmetric HI kinematics tend to have asymmetric stellar morphology and kinematics as well, suggesting a tidally induced lopsidedness. On the other hand, galaxies with symmetric HI morphology and asymmetric HI kinematics tend to have symmetric stellar morphology and kinematics, suggesting a gas accretion-induced lopsidedness whose signature appears stronger in the gas kinematics or that the gas kinematics retains non-axisymmetric signatures longer. In the following section, we study the evolution of

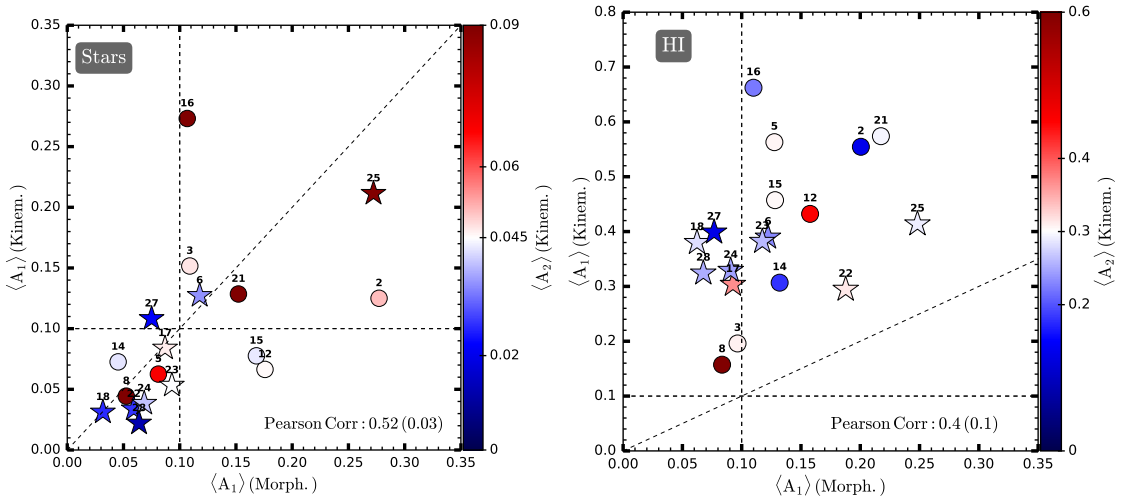


Fig. 7. Present-day global kinematical lopsidedness compared with the present-day global morphological lopsidedness of the stellar (*left*) and HI (*right*) disks of the nine Superstars and nine L4 galaxies. The value of the Pearson coefficient quantifying the strength of the correlation is reported in each figure, with the p-value indicated within brackets. The symbols have the same meaning as in Fig. 3. Markers are color coded by the corresponding amplitude of the $m = 2$ Fourier mode calculated from the face-on projected present-day radial velocity maps of the stellar and HI disks between 0.5 and 1 $R_{\rm opt}$. The global morphological and kinematical lopsidedness have been measured for both stars and HI as described in Sects. 3.1 and 3.2, respectively, over the same spatial extent. The diagonal dashed line indicates the one-to-one relation, while the vertical and horizontal dashed lines represent the lopsidedness threshold $\langle A_{1,\rm kin}\rangle = \langle A_1\rangle = 0.1$.

lopsidedness in the Superstars galaxies and its connection to past interactions with the aim of identifying the dominant mechanisms driving the observed morphological and kinematical asymmetries.

4. Drivers of lopsidedness in Superstars

In order to understand the origin of lopsidedness, we studied its evolution as a function of time. We focus here on the morphological lopsidedness in a time window covering the past 7 Gyr of galactic history up to the present-day. We did not go back to earlier times where there is not yet a well-formed disk. In Fig. 8, we show the global $\langle A_1\rangle$ of the stellar and HI disks as a function of lookback time for the nine Superstars galaxies. We also show the time evolution of the global $\langle A_1\rangle$ of the young stellar component (<0.5 Gyr ago). We measure $\langle A_1\rangle$ using the method described in Sect. 3.1, after determining the optical radius $R_{\rm opt}$ and the disk height h_{90} of the stellar disk at each time (see Sect. 2.3.1). This ensures that the global $\langle A_1\rangle$ of both the stellar and HI gas components is measured over the same spatial region, defined by the stellar disk extent at each time (i.e., between 0.5 and 1 $R_{\rm opt}$ and within a vertical extent of $2|h_{90}|$ from the galactic plane). For each galaxy, in Fig. 8, we also show the relative distance of the most significant interacting and merging satellites over the last 7 Gyr from the center of the main host galaxy at each time. Distances are normalized by the virial radius R_{200} of the main host at each time. The satellite orbits are color coded by the total mass of the satellite galaxy at each time. We consider only satellite galaxies with a total mass ratio >1:50 at the time they first cross the virial radius R_{200} of the main host. Furthermore, we show the satellite orbits only until their total mass drops below $M_{\rm tot} = 10^9\,M_\odot$.

4.1. Present-day lopsided galaxies

In Fig. 8, we see that the two present-day lopsided galaxies with consistent stellar and HI gas density asymmetries at $z = 0$ (i.e., Au6 and Au25; see Sect. 3.3) also show very good agreement between the global $\langle A_1\rangle$ of the stellar and HI gas components at all earlier times over the last 7 Gyr. In particular, Au25 shows a mildly decreasing $\langle A_1\rangle$ amplitude over most of its recent history, followed by a steep increase during the last 1 Gyr up to the present day, consistently in both the stellar and HI gas components. This sharp rise in $\langle A_1\rangle$ occurs just before the deep pericentric passage, ∼1 Gyr ago, of a massive satellite galaxy with a total mass ratio in the range 1:4-1:3 at the time it first crossed the R_{200} of the main host, meaning that the interaction already starts affecting the galaxy morphology before the pericentric passage. In Fig. C.1 we show a snapshot sequence to visualize the time of this significant interaction within the last ∼1 Gyr ago. We therefore conclude that the present-day morphological lopsidedness of Au25 is the result of a tidal interaction with a massive satellite that still survives at $z = 0$ and perturbed both the stellar and HI gas density distributions. In previous works, Gómez et al. (2017) showed that this strong interaction also caused a misalignment between the outer dark matter halo and the inner disk in this galaxy using the original Auriga simulation, while Grand et al. (2026) showed that strong two-armed spirals arise from this interaction using the Superstars simulation.

In contrast, Au6 shows two prominent $\langle A_1\rangle$ peaks at ∼5 and ∼2 Gyr ago in both the stellar and HI gas components, indicating that lopsidedness is triggered multiple times in this galaxy. As in the case of Au25, the earlier $\langle A_1\rangle$ peak of Au6 at ∼5 Gyr ago is associated with an interacting satellite with total mass ratio in the range 1:50-1:20 at the time it first crossed the R_{200} of the main host. This satellite underwent multiple deep pericentric passages around 6 Gyr ago, during which its total mass remains above $10^9\,M_\odot$, perturbing both the stellar and HI gas density distributions. Subsequently, the satellite continues orbiting the main host but has lost most of its mass ($M_{\rm tot} < 10^9\,M_\odot$), which is why it does not appear in the bottom panel of Fig. 8. It eventually merges with the host ∼0.5 Gyr ago, without inducing significant additional perturbations. The more recent $\langle A_1\rangle$ peak ∼2 Gyr ago of Au6 also coincides with the close passage of a fly-by satellite with a total mass ratio slightly greater than 1:20 at the time of

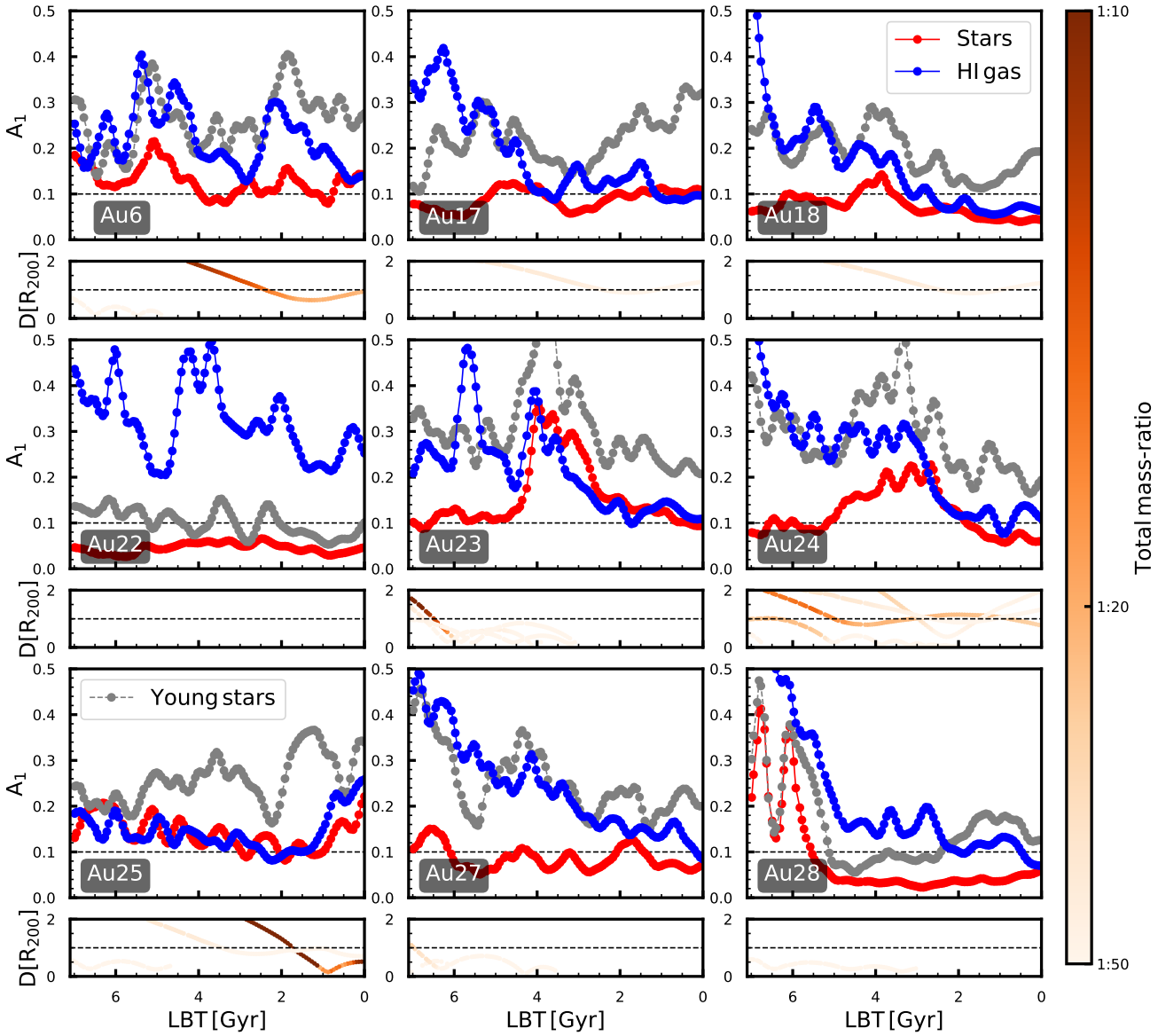


Fig. 8. Global morphological lopsidedness of the stellar (red curve) and HI (blue curve) disks as a function of lookback time of the nine Superstars galaxies. We consider a time window between the present day and 7 Gyr ago. We also show the time evolution of the global morphological lopsidedness of the young stellar component (<0.5 Gyr; gray curve). A small Gaussian smoothing ($\sigma \sim 130$ Myr) has been applied to the lopsidedness curves of each component. The horizontal dashed line represents the lopsidedness threshold $\langle A_1 \rangle = 0.1$. The small rectangular panel below each galaxy shows the relative distance of the most significant interacting and merging satellites over the last 7 Gyr from the center of the main host galaxy at each time. Distances have been normalized by the virial radius R_{200} of the main host at each time and are shown in linear scale. The satellite orbits are color coded by the total mass of the satellite galaxy at each time. We only considered satellite galaxies with a total mass ratio > 1:50 at the time they first crossed the virial radius R_{200} of the main host. Furthermore, we show the satellite orbits only until their total mass drops below $M_{tot} = 10^9\,M_\odot$.

first R_{200} crossing. However, in this case, the satellite does not penetrate deeper than $0.5\,R_{200}$. In Fig. C.2 we show the snapshot sequence of the fly-by passage of this massive satellite. As a result, the lopsided distribution observed in both the stellar and HI gas density fields may have been induced by dark matter density wakes generated in the halo of the main host by the orbiting satellite (Gómez et al. 2016; Garavito-Camargo et al. 2019; Grand et al. 2023). In this scenario, the lopsidedness arises from the response of the disk to the perturbed dark matter halo potential. We will verify this scenario in a follow-up work. Observational studies have reported that the Milky Way has a lopsided HI gas distribution at large galactocentric radii (i.e., $\gtrsim$15 kpc) in the direction of the Magellanic Clouds, suggesting that this asymmetry is the result of a dark matter wake induced by this satellite system (Kalberla & Dedes 2008).

We note that both Au6 and Au25 are characterized by a lower-than-average central stellar mass density, μ_* (see Fig. 3). For this reason, even the fly-by passage of a lower-mass satellite is likely to induce small perturbations in both the stellar and HI gas density fields.

One interesting difference between Au6 and Au25 concerns the behavior of the young stellar component (i.e., <0.5 Gyr old). In Au6, we find a close correspondence between the lopsidedness amplitudes of the HI gas, young stars, and the total stellar component, suggesting that the gravitational perturbations trigger a coherent response across all components. In contrast, in

Au25, we find that the young stellar component is already more strongly lopsided at earlier times (~6–2 Gyr ago), while both the HI gas and the total stellar component are more weakly lopsided. Inspection of the surface density maps suggests that this behavior reflects the fact that young stars trace asymmetric star formation along the strong spiral arms, meaning that there is more star formation in one of the spirals compared to the other for a two-armed spiral. Therefore, the young stellar component provides a more sensitive tracer of localized, non-axisymmetric overdensities associated with the spiral pattern. This is consistent with the recent work of Grand et al. (2026) who, using the Auriga Superstars simulation, showed that spiral structure can arise as a result of different dynamical processes and evolve on sub-Gyr timescales, leading to significant variations in the morphology and strengths of spiral arms.

4.2. Present-day symmetric galaxies

4.2.1. Galaxies with early stellar and HI gas lopsidedness

Among the present-day symmetric galaxies, Au23, Au24, and Au28 show strong lopsidedness in both stellar and HI gas components at earlier times, i.e., between ~5 and 2 Gyr ago for Au23 and Au24, and at >5 Gyr ago for Au28. In the case of Au23, only the HI gas density distribution is lopsided at epochs earlier than 5 Gyr ago as a result of smooth gas accretion from two gas-rich fly-by satellites from ~6 Gyr ago with total mass ratios between 1:50 and 1:10 at the time of their first R_{200} crossing. This gas accretion likely triggers asymmetric star formation, which is traced by the young stellar population. The most massive of the previous two satellites (i.e., total mass ratio ~1:10 at the time of first R_{200} crossing) later interacts more strongly with the main host during a second pericentric passage at ~4 Gyr ago, producing a coherent lopsided perturbation in the density distributions of the HI gas, young stars, and the total stellar component. In Fig. C.3 the sequence of snapshots at ~6 Gyr ago (top panels) indicates the epoch of the early gas accretion-induced lopsidedness, while the sequence of snapshots at ~4 Gyr ago (bottom panels) shows the subsequent significant interaction from a massive satellite. Subsequently, the galaxy does not experience any further significant interactions, leading to a gradual damping of its lopsidedness across all components. Using a larger statistical sample from the IllustrisTNG (TNG50) simulation, Fontirroig et al. (2025) showed that ~20% of galaxies underwent an early interaction (~6.5 Gyr ago) with a massive satellite (mass ratio > 1:20) that triggered a prominent lopsided perturbation. However, at later times, this lopsidedness gradually decreased and the galaxies eventually became symmetric in the absence of further external interactions (see figure 9 of Fontirroig et al. 2025), as we observe for Au23 in this work.

Similarly, Au24 experiences smooth gas accretion from fly-by satellites with total mass ratios of ~1:20 at the time of their first R_{200} crossing at early times (≳5 Gyr ago), which primarily perturbs the HI gas density distribution and likely triggers asymmetric star formation traced by the young stellar population. At later times, these satellites produce a coherent lopsided perturbation in the density distributions of the HI gas, young stars, and the total stellar components during their subsequent pericentric passages between ~5 and 2 Gyr ago, while continuing to accrete gas onto the main host. At more recent times (i.e., ≲2 Gyr ago), Au24 only experienced minor interactions with satellites of total mass ratios ~1:50 at the time of their first R_{200} crossing. However, these satellites' interactions do not induce further significant perturbations due to the fact that Au24 has an above-average central stellar mass density (see Fig. 3). As a result, there is a gradual decrease in lopsidedness across all components.

In contrast, Au28 experiences a significant interaction with a massive satellite (total mass ratio ~1:20 at the time of its first R_{200} crossing) at early times (~6 Gyr ago), which coherently perturbs the density distributions of the HI gas, young stars, and the total stellar component. Following this event, the galaxy undergoes a relatively quiescent evolutionary phase, without further significant interactions and only minor smooth accretion from very low-mass satellites (total mass ratios <1:50 at the time of their first R_{200} crossing). The lack of significant interactions, combined with the high central stellar mass density of this galaxy (see Fig. 3), leads to a rapid decrease in lopsidedness in the stellar component and a more gradual damping of lopsidedness in the HI gas component toward the present-day.

4.2.2. Galaxies with only HI gas lopsidedness

Finally, the remaining four present-day symmetric galaxies (i.e., Au17, Au18, Au22, and Au27) maintain an overall symmetric stellar disk throughout their evolution, as shown in Fig. 8. In particular, three galaxies (i.e., Au17, Au18, and Au27) exhibit an early perturbation in the HI gas density distribution (≳4 Gyr ago), which is gradually damped toward the present-day, whereas Au22 maintains a perturbed HI gas density distribution with an approximately constant $\langle A_1 \rangle$ throughout its evolution history.

In the case of Au17 and Au18, no significant interactions with nearby satellites occur at early times between ~7–4 Gyr ago. These galaxies are also characterized by above-average central stellar mass densities (see Fig. 3), which likely stabilizes their stellar disk against external perturbations. For this reason, they maintain an overall symmetric stellar disk, while the lopsidedness in their HI gas density distributions is likely driven by the asymmetric smooth gas accretion from the cosmic web or low-mass satellites. In Fig. C.4 we show a sequence of six snapshots displaying the time evolution between ~7 to 4 Gyr ago for Au17, as an example. The images confirm that this galaxy did not experience any significant interactions with any massive satellite at early times (i.e., ≳4 Gyr ago). Nonetheless, the HI gas disk shows significant perturbations up to ~5 Gyr ago compared to the stellar disk, which remains mostly symmetric. This is consistent with the hypothesis that the HI disk asymmetry is induced by smooth gas accretion, as mentioned above. This process may also trigger asymmetric star formation, traced by the young stellar population. We will further test this gas accretion scenario in a follow-up work. At later times, both galaxies experience the pericentric passage (~2 Gyr ago) of a satellite with a total mass ratio of ~1:50 at the time of its first R_{200} crossing. However, because of the low satellite mass, its shallow penetration into the main host R_{200}, and the relatively high central stellar mass density of these galaxies, this fly-by does not induce significant perturbations in either the stellar or HI disks. Only the young stellar component becomes mildly lopsided at these times, tracing localized, non-axisymmetric overdensities associated with the spiral pattern, similarly to Au25.

A similar scenario also applies to Au22, which has not experienced any significant interactions or mergers within the last 7 Gyr. The lack of strong interactions, combined with the very high central stellar mass density of this galaxy, likely explains why it exhibits the most symmetric stellar disk throughout its history. In this case, continuous smooth gas accretion, from either the cosmic web or low-mass satellite galaxies, likely produces the lopsided HI mass distribution, while both the total

and young stellar components trace the underlying smooth mass distribution of the compact stellar disk with no prominent spiral arms. Alternatively, the strong AGN activity presents in this galaxy could be an additional source of perturbation of its HI gas distribution (Grand et al. 2017). In a follow-up study, we will test the gas accretion scenario by using tracer particles to track the time evolution of gas cells in these galaxies.

In contrast, Au27 undergoes several pericentric passages from a gas-rich satellite with a total mass ratio between 1:50 and 1:20 at the time of its first R_{200} crossing between ∼7–4 Gyr ago. These interactions primarily perturb the density distribution of the HI gas and likely trigger asymmetric star formation, traced by the young stellar population that closely follows the HI gas distribution. The total stellar disk remains largely unaffected, likely due to its relatively high central stellar mass density, which stabilizes it against such perturbations. At later times, Au27 mainly experiences smooth accretion from low-mass satellites (total mass ratios $\lesssim$1:50 at the time of their first R_{200} crossing), leading to a gradual decrease in lopsidedness in the density distributions of both the HI gas and the young stellar population.

5. Summary and conclusions

In this work, we have characterized the lopsidedness in both the density and kinematics of the stellar and HI gas components of a sample of nine Milky Way-type galaxies from the Auriga Superstars cosmological zoom-in simulations as well as of a sample from the original Auriga simulations. We quantified both morphological and kinematical lopsidedness, as described in Sects. 3.1 and 3.2. From the analysis of the correlation between global morphological lopsidedness in the stellar and HI gas components as well as the correlation between global morphological and kinematical lopsidedness in both the stellar and HI gas components at $z = 0$, we report the following results:

- Within the stellar optical radius $R_{\rm opt}$, we find that an asymmetry in the stellar density distribution is generally accompanied by a corresponding asymmetry in the HI gas density distribution, but the opposite is not necessarily true. In particular, we find that the old stellar component (>0.5 Gyr old) is strongly coupled with the HI gas such that high $\langle A_1 \rangle$ in the stars corresponds to high $\langle A_1 \rangle$ in the HI gas, making it a tracer of asymmetries in the overall mass distribution of galaxies. In contrast, the young stellar component (<0.5 Gyr old) is sensitive to asymmetric star formation along the strong spiral arms. These results are discussed in Sect. 3.3.1.
- Morphological and kinematical lopsidedness in the stellar component are also correlated, as expected if lopsidedness arises from a perturbed gravitational potential that coherently affects both stellar orbits and their spatial distribution and consistent with the results from previous numerical simulations (Ghosh et al. 2025). In contrast, we find only a weak correlation between morphological and kinematical lopsidedness in the HI gas, which is typically characterized by stronger kinematical than morphological asymmetries. Taken together, these results suggest that independent of whether lopsidedness is tidally and/or gas accretion-induced, its imprint is stronger in the HI gas kinematics than in its morphology (as described in Sect. 3.4.1).
- As shown in Fig. 5, we found an anticorrelation between lopsidedness in the stellar density distribution of the outer galactic disk and the bar strength in the inner regions. Namely, galaxies with stronger bars (i.e., high $\langle A_2 \rangle$) tend to have lower lopsided amplitudes (i.e., low $\langle A_1 \rangle$), whereas galaxies with weaker bars (i.e., low $\langle A_2 \rangle$) tend to have higher lopsided amplitudes (i.e., high $\langle A_1 \rangle$). In particular, the most strongly barred galaxies are also characterized by a high central stellar mass density, whereas lopsided galaxies typically have a low central stellar mass density. For this reason, we conclude that the anticorrelation between lopsidedness and bar strength is a result of the strong correlation of both quantities with the galaxy central stellar mass density, as galaxies with a high central stellar mass density tend to be less susceptible to developing lopsided perturbations while being more likely to host strong bars. These conclusions are further supported by previous works, which have shown that the galaxy central stellar mass density is a key parameter for determining whether a galaxy is more susceptible to developing lopsidedness and/or a bar (Fragkoudi et al. 2025; Fontirroig et al. 2025).

Additionally, from the analysis of the time evolution of lopsidedness in the stellar and HI gas density distributions of the Superstars galaxies (see Sect. 4), we find the following results:

- A close correspondence between peaks in the global $\langle A_1 \rangle$ of the stellar and HI gas components is typically associated with the pericentric passage of a massive satellite (total mass ratio >1:50 at the time of first R_{200} crossing), which triggers a coherent response across all components. However, whether lopsidedness arises through the direct physical encounter or through the indirect response of the disk to the perturbed dark matter halo will be explored in a follow-up work. We found that in five out of the nine galaxies, lopsidedness is triggered by a tidal encounter (i.e., Au6, Au23, Au24, Au25, and Au28).
- A lopsided density distribution only in the HI gas is generally consistent with smooth gas accretion, either from gas-rich fly-by satellites or from the cosmic web. We found that in six out of nine galaxies, lopsidedness is triggered by smooth gas accretion (i.e., Au17, Au18, Au22, Au23, Au24, and Au27). When lopsidedness is driven by gas accretion, the HI gas and young stars show similar lopsided amplitudes, while the total stellar distribution remains largely symmetric.
- When only the young stellar population is lopsided, this is indicative of asymmetric star formation along strong spiral arms (e.g., Au17 and Au25). Therefore, the young stellar component can act as a sensitive tracer of localized non-axisymmetric overdensities associated with the spiral pattern. However, when only the HI gas is lopsided at all times (e.g., Au22), it likely indicates smooth gas accretion or strong AGN activity.

One interesting finding is that lopsidedness over a galaxy evolutionary history can be driven by a combination of both processes. Gas accretion from a fly-by satellite may first produce lopsidedness only in the HI gas component, while a subsequent tidal interaction with the same or another satellite can later produce lopsidedness in all components (i.e., stars and HI gas). Specific examples of this include Au23 and Au24.

Although in this work we quantified the intrinsic lopsidedness of galaxies using face-on projections to measure the lopsidedness of the stellar and HI gas components individually and we characterized the kinematical lopsidedness using the radial component of the velocity rather than the line-of-sight velocity accessible in observations, our results can still provide a useful framework for interpreting observational studies. In particular, we find that a coherent lopsided response in both the stellar and HI gas components is indicative of a global perturbation to the gravitational potential, such as that induced by a tidal interaction, producing both morphological and kinematical

asymmetries. In contrast, a lopsided response only in the HI gas component (and possibly in the young stellar component) is indicative of such processes as asymmetric gas accretion from either the cosmic web or low-mass satellites, which primarily affect the morphology and kinematics of the gas while leaving the old stellar component largely unperturbed. Therefore, the combined analysis of morphological and kinematical lopsidedness across multiple tracers, such as stars and HI gas, can provide valuable information for distinguishing between the different mechanisms triggering the disk lopsidedness, thus allowing the recent evolutionary histories of galaxies to be constrained. A more quantitative comparison with observations, including the use of line-of-sight velocity maps, is beyond the scope of this work and will be left to a future study.

In a follow-up work, we will also investigate in more detail the role of gas accretion as a driving mechanism of lopsidedness in disk galaxies. By tracking gas cells in the Auriga Superstars simulations, we aim to distinguish accretion from the cosmic web, from satellite galaxies, and from recycled gas associated with galactic fountain flow (Grand et al. 2019) and to measure the direction of gas inflows. This will allow us to determine the origin of gas accretion, determine whether this inflow occurs asymmetrically, and assess how such accretion is connected to the observed coupling or decoupling of lopsidedness in the HI gas, young stellar population, and total stellar components.

Acknowledgements. We thank the anonymous referee for their constructive comments and suggestions that helped to improve this paper. AD acknowledges support from the FONDECYT Postdoctorado No. 3250558. RB is supported by the SNSF through the Ambizione Grant PZ00P2_223532. RJJG is supported by an STFC Ernest Rutherford Fellowship (ST/W003643/1). FAG and AM acknowledge support from the ANID BASAL project FB210003, and funding from the HORIZON-MSCA-2021-SE-01 Research and Innovation Programme under the Marie Sklodowska-Curie grant agreement number 101086388. FAG acknowledges support from the ANID FONDECYT Regular grant 1251493. AM acknowledges support from the ANID FONDECYT Regular grant 1251882. FvdV is supported by a Royal Society University Research Fellowship (URF\R1\191703 and URF\R\241005).

References

Angiras, R. A., Jog, C. J., Omar, A., & Dwarakanath, K. S. 2006, MNRAS, 369, 1849
Angiras, R. A., Jog, C. J., Dwarakanath, K. S., & Verheijen, M. A. W. 2007, MNRAS, 378, 276
Baldwin, J. E., Lynden-Bell, D., & Sancisi, R. 1980, MNRAS, 193, 313
Beale, J. S., & Davies, R. D. 1969, Nature, 221, 531
Bekki, K., & Couch, W. J. 2011, MNRAS, 415, 1783
Bilimogga, P. V., Busekool, E., Verheijen, M. A. W., & van der Hulst, J. M. 2026, A&A, 710, A159
Blitz, L., & Rosolowsky, E. 2006, ApJ, 650, 933
Block, D. L., Bertin, G., Stockton, A., et al. 1994, A&A, 288, 365
Bosma, A. 1981, AJ, 86, 1791
Bournaud, F., Combes, F., & Jog, C. J. 2004, A&A, 418, L27
Bournaud, F., Combes, F., Jog, C. J., & Puerari, I. 2005, A&A, 438, 507
Deeley, S., Drinkwater, M. J., Sweet, S. M., et al. 2021, MNRAS, 508, 895
Dolfi, A., Gómez, F. A., Monachesi, A., et al. 2023, MNRAS, 526, 567
Dolfi, A., Gómez, F. A., Monachesi, A., et al. 2025, A&A, 699, A11
Faucher-Giguère, C.-A., Lidz, A., Zaldarriaga, M., & Hernquist, L. 2009, ApJ, 703, 1416
Feng, S., Shen, S., Chen, Y., et al. 2025, ApJ, 995, 18
Fontirroig, V., Gómez, F. A., Jaque Arancibia, M., Dolfi, A., & Monsalves, N. 2025, A&A, 699, A118
Fragkoudi, F., Grand, R. J. J., Pakmor, R., et al. 2025, MNRAS, 538, 1587
Garavito-Camargo, N., Besla, G., Laporte, C. F. P., et al. 2019, ApJ, 884, 51
Ghosh, S., Di Matteo, P., Jog, C. J., & Frankel, N. 2025, ArXiv e-prints [arXiv:2511.07549]
Gómez, F. A., White, S. D. M., Marinacci, F., et al. 2016, MNRAS, 456, 2779
Gómez, F. A., White, S. D. M., Grand, R. J. J., et al. 2017, MNRAS, 465, 3446
Grand, R. J. J., Gómez, F. A., Marinacci, F., et al. 2017, MNRAS, 467, 179
Grand, R. J. J., van de Voort, F., Zjupa, J., et al. 2019, MNRAS, 490, 4786
Grand, R. J. J., Pakmor, R., Fragkoudi, F., et al. 2023, MNRAS, 524, 801
Grand, R. J. J., Fragkoudi, F., Gómez, F. A., et al. 2024, MNRAS, 532, 1814
Grand, R. J. J., Fragkoudi, F., Pakmor, R., et al. 2026, MNRAS, 548, stag774
Haynes, M. P., Hogg, D. E., Maddalena, R. J., Roberts, M. S., & van Zee, L. 1998, AJ, 115, 62
Ikeuchi, S., & Ostriker, J. P. 1986, ApJ, 301, 522
Jog, C. J. 1997, ApJ, 488, 642
Jog, C. J. 2002, A&A, 391, 471
Jog, C. J., & Combes, F. 2009, Phys. Rep., 471, 75
Kalberla, P. M. W., & Dedes, L. 2008, A&A, 487, 951
Katz, N., Hernquist, L., & Weinberg, D. H. 1992, ApJ, 399, L109
Katz, N., Weinberg, D. H., & Hernquist, L. 1996, ApJS, 105, 19
Le Bail, A., Daddi, E., Elbaz, D., et al. 2024, A&A, 688, A53
Leroy, A. K., Walter, F., Brinks, E., et al. 2008, AJ, 136, 2782
Łokas, E. L. 2022, A&A, 662, A53
Manuwal, A., Ludlow, A. D., Stevens, A. R. H., Wright, R. J., & Robotham, A. S. G. 2022, MNRAS, 510, 3408
Marinacci, F., Grand, R. J. J., Pakmor, R., et al. 2017, MNRAS, 466, 3859
Nelson, D., Springel, V., Pillepich, A., et al. 2019, Comput. Astrophys. Cosmol., 6, 2
Noordermeer, E., Sparke, L. S., & Levine, S. E. 2001, MNRAS, 328, 1064
Pakmor, R., Bieri, R., Fragkoudi, F., et al. 2025a, MNRAS, 543, 1761
Pakmor, R., Fragkoudi, F., Grand, R. J. J., et al. 2025b, MNRAS, 543, 4355
Planck Collaboration XVI. 2014, A&A, 571, A16
Reichard, T. A., Heckman, T. M., Rudnick, G., Brinchmann, J., & Kauffmann, G. 2008, ApJ, 677, 186
Richter, O.-G., & Sancisi, R. 1994, A&A, 290, L9
Rix, H.-W., & Zaritsky, D. 1995, ApJ, 447, 82
Schoenmakers, R. H. M., Franx, M., & de Zeeuw, P. T. 1997, MNRAS, 292, 349
Smith, R., Fellhauer, M., & Assmann, P. 2012, MNRAS, 420, 1990
Springel, V. 2010, MNRAS, 401, 791
Springel, V., & Hernquist, L. 2003, MNRAS, 339, 289
Swaters, R. A., Schoenmakers, R. H. M., Sancisi, R., & van Albada, T. S. 1999, MNRAS, 304, 330
Varela-Lavin, S., Gómez, F. A., Tissera, P. B., et al. 2023, MNRAS, 523, 5853
Vogelsberger, M., Genel, S., Sijacki, D., et al. 2013, MNRAS, 436, 3031
Weinberg, M. D. 1995, ApJ, 455, L31
Wilcots, E. M. 2010, ASP Conf. Ser., 421, 149
Zaritsky, D., & Rix, H.-W. 1997, ApJ, 477, 118

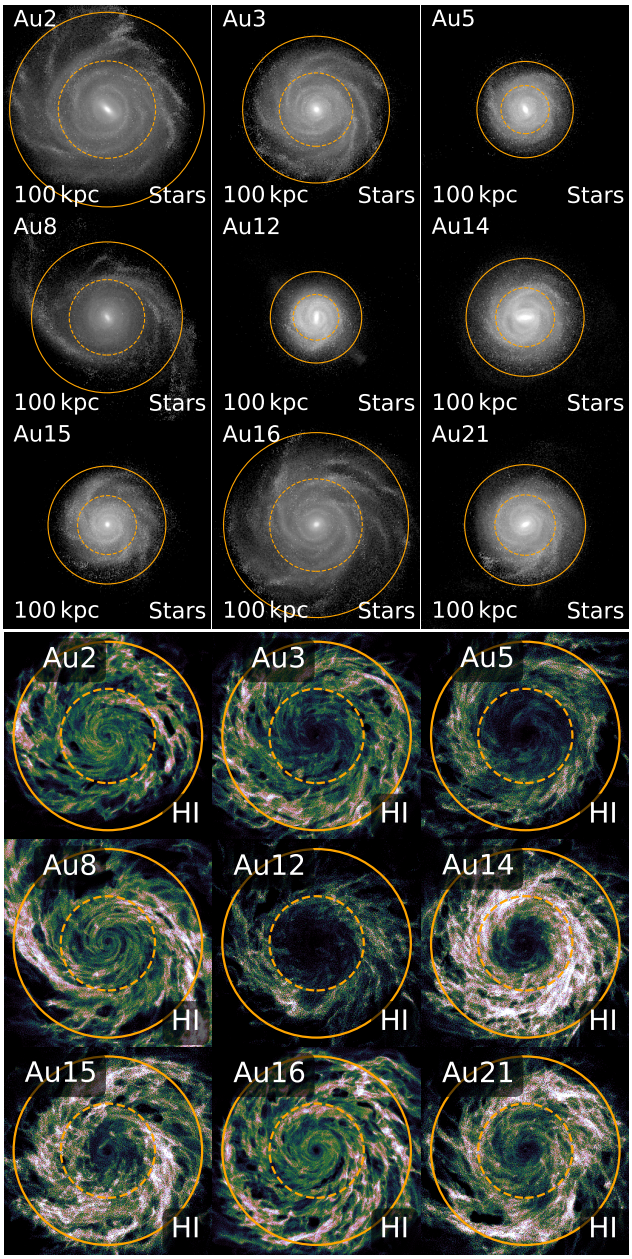


Fig. A.1. *Top panels:* Present-day face-on V-band stellar surface brightness maps of the nine original Auriga (L4) galaxies at $z = 0$. The dashed and solid orange circles define the region at 0.5 and 1 $R_{\rm opt}$, respectively, where $R_{\rm opt}$ is calculated as described in Sect. 2.3.1. The extent of each image, centered on the galaxy, ranges from $-2\,R_{\rm opt}$ to $+2\,R_{\rm opt}$ along both axes. *Bottom panels:* Same but showing the present-day face-on HI surface density maps.

Appendix A: Original Auriga galaxies

In Fig. A.1, we show the face-on projection of the present-day V-band stellar surface brightness maps (left panels) and of the HI surface density maps (right panels) of the nine original Auriga (L4) galaxies at $z = 0$ with D/T ≥ 0.5, which are included in this work when studying global galaxy properties (see Sects. 2.1 and 3). In Table A.1, we summarize the main properties at $z = 0$ of these nine Auriga galaxies, along with their values of the present-day global morphological and kinematical lopsidedness for both stars and HI gas.

Table A.1. Properties of original Auriga (L4) galaxies.

ID	M_* ($10^{10}\,M_\odot$)	$M_{\rm HI}$ ($M_\odot$)	$R_{\rm opt}$ (kpc)	M_{200} ($10^{12}\,M_\odot$)	$\langle A_1 \rangle$ (Stars - HI)	$\langle A_{1,\rm kin} \rangle$ (Stars - HI)
Au2	9.42	2.15	46.8	1.91	0.27 – 0.20	0.12 – 0.55
Au3	8.72	1.59	35.3	1.45	0.10 – 0.09	0.15 – 0.19
Au5	7.12	0.46	23.1	1.18	0.08 – 0.12	0.06 – 0.56
Au8	3.96	2.56	36.3	1.08	0.05 – 0.08	0.04 – 0.15
Au12	6.61	0.37	21.9	1.09	0.17 – 0.15	0.06 – 0.43
Au14	11.73	1.81	28.4	1.65	0.04 – 0.13	0.07 – 0.30
Au15	4.33	1.49	28.3	1.22	0.16 – 0.12	0.07 – 0.45
Au16	7.02	2.90	44.5	1.50	0.10 – 0.10	0.27 – 0.66
Au21	8.66	1.68	29.0	1.45	0.15 – 0.21	0.12 – 0.57

Notes. Main properties of the nine original Auriga (L4) galaxies at $z = 0$. Column from left to right: the galaxy ID, the total galaxy stellar mass (M_*), the total galaxy HI gas mass ($M_{\rm HI}$), the stellar optical radius in the V-band ($R_{\rm opt}$), the halo mass (M_{200}), the galaxy global morphological lopsidedness for both stars and HI gas ($\langle A_1 \rangle$), and the galaxy global kinematical lopsidedness for both stars and HI gas ($\langle A_{1,\rm kin} \rangle$).

Appendix B: Stellar mass distribution across models and resolution

In this section we first study whether the improved stellar particle mass resolution of Superstars has a significant impact on the overall stellar mass distribution within the galactic disk at $z = 0$. For each Superstars galaxy (see Sect. 2.3), we consider its low resolution counterpart in L4. For both sets of galaxies, we calculate the optical radius (i.e., $R_{\rm opt}^{\rm SStar}$ and $R_{\rm opt}^{\rm L4}$) and disk height (i.e., $h_{90}^{\rm SStar}$ and $h_{90}^{\rm L4}$), as described in Sect. 2.3.1. We then calculate the average values of $< R_{\rm opt} >$ and $< h_{90} >$ between the Superstars and L4 resolutions for each galaxy[3]. We use these average values to define the extension of the stellar disk, and the spatial region over which the lopsidedness is measured in both the Superstars and L4 resolutions.

In the top panels of Fig. B.1, we show the present-day lopsided profiles of each Superstars galaxy at both the Superstars and L4 resolution, while, in the bottom panels, we show the difference between the lopsided profiles measured at the Superstars and L4 resolutions. We also calculate the root-mean-square-error (RMSE) to quantify the overall difference between the lopsided profiles. In the bottom panels of Fig. B.1, we see that the difference $A_1^{\rm SStar} - A_1^{\rm L4}$ between the lopsided profiles measured in the Superstars and L4 resolutions show only moderate local variations as a function of radius ($\lesssim 0.02$). We find an overall good agreement between the lopsided profiles of the galaxies in Superstars and L4, as suggested by the small RMSE $\lesssim 0.05$. Only one galaxy (i.e., Au6) shows a larger RMSE $\simeq 0.07$, but the shapes of the lopsided profiles in Superstars and L4 still show good agreement. In fact, we find that the strongly lopsided galaxies in Superstars are also strongly lopsided in L4 (e.g., Au25; $A_1 >> 0.1$), while the strongly symmetric galaxies in Superstars are also strongly symmetric in L4 (e.g., Au18; $A_1 << 0.1$), as suggested by the comparable $\langle A_1 \rangle$ values calculated for each galaxy. Weakly perturbed galaxies in Superstars with $\langle A_1 \rangle$ values close to the threshold $\simeq 0.1$ also show similar weakly perturbed lopsided profiles in L4 (i.e., Au17, Au23, Au24, and Au27). Furthermore, we note that the Superstars galaxies have always generally the same (Au28) or slightly smaller $\langle A_1 \rangle$ than the original

[3] We note that the individual values of $R_{\rm opt}$ and h_{90} are generally similar between the Superstars and L4 simulations

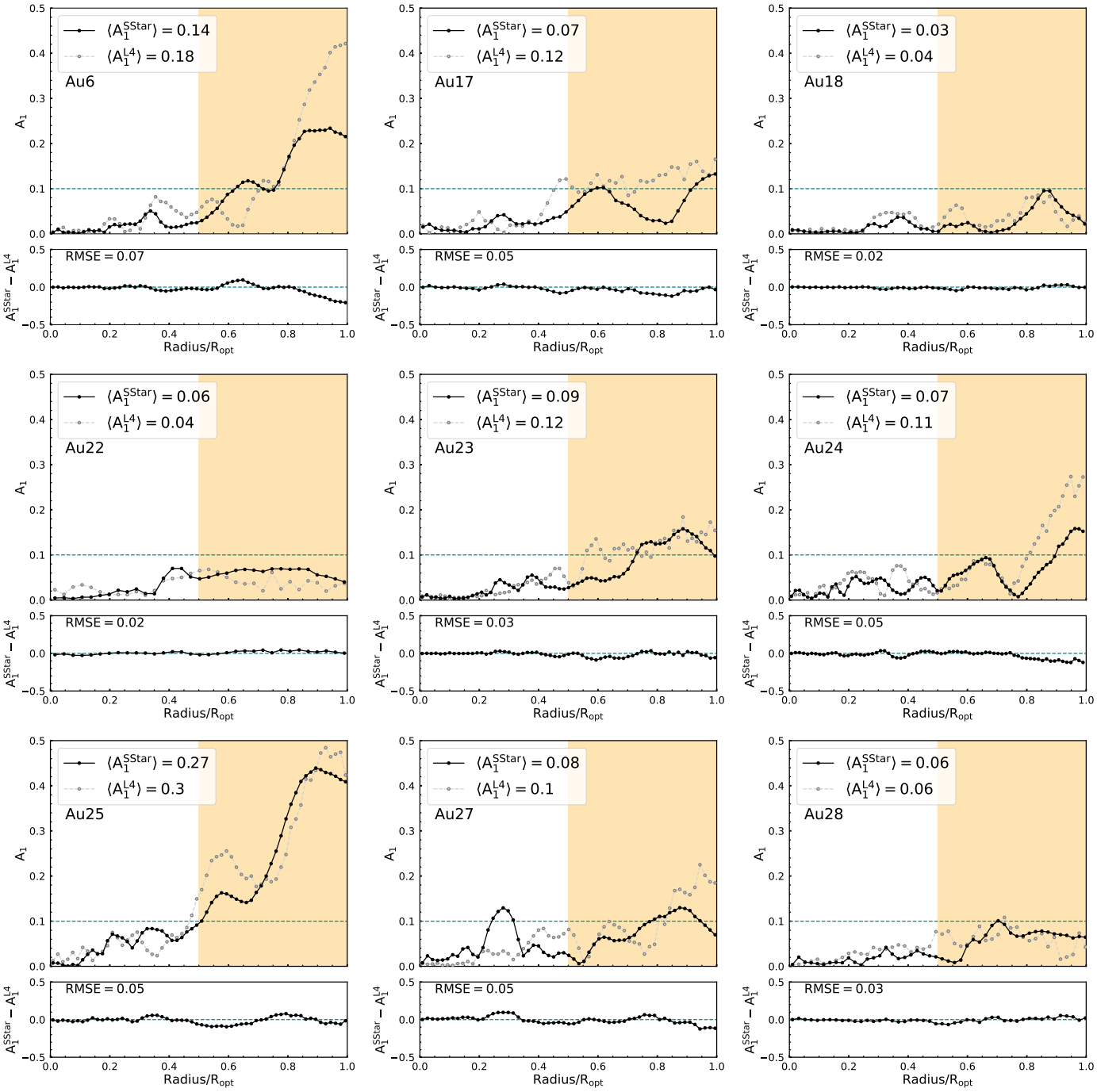


Fig. B.1. *Top panels:* Present-day lopsided profiles of stellar mass density of the nine galaxies in Superstars (black lines) compared with their corresponding low-resolution counterpart in the original Auriga simulations from Grand et al. (2017) (gray lines). The horizontal dashed line indicates the lopsidedness threshold $\langle A_1 \rangle = 0.1$, while the shaded orange region represents the radial interval between 0.5-1 $R_{\rm opt}$ used to quantify the global lopsidedness of the stellar disk. The resulting global $\langle A_1 \rangle$ is shown in the legend for each galaxy at both the Superstars and L4 resolution. *Bottom panels:* For each galaxy, we compute the difference between the lopsided profiles measured in Superstars and L4 at each radius and calculate the root mean square error to quantify the overall variation.

lower resolution L4 galaxies. This indicates that noise can affect the lopsidedness measurement, as we see that the L4 lopsided profiles are noisier at large radii than the Superstars lopsided profiles.

For each Superstars galaxy, we also calculate the present-day central stellar mass density[4] and we compare it with that measured in the L4 counterpart. Similarly to Fig. B.1, we use the average value of the half-mass radius $\langle R_{\rm h} \rangle$, calculated between the Superstars and L4 resolutions for each galaxy, to define the

[4] The central stellar mass density is defined as $\mu_* = M_{*,\rm h}/\pi R_{\rm h}^2$, where $M_{*,\rm h}$ is the stellar mass enclosed within an area delimited by the stellar half-mass radius $R_{\rm h}$ of the galaxy.

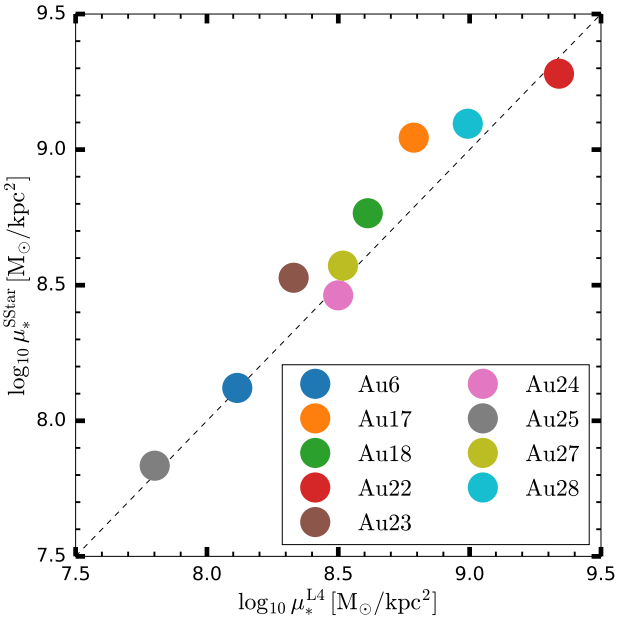


Fig. B.2. Present-day central stellar mass density of the nine galaxies in Superstars compared with the central stellar mass density of the same galaxies at the L4 resolution. The diagonal dashed black line indicates the one-to-one relation.

inner galactic regions where the central stellar mass density is measured in both Superstars and L4 resolutions. The results are shown in Fig. B.2. We find that there is a very good agreement between the central stellar mass density in Superstars and L4 at $z = 0$ (i.e., all galaxies typically lie along the one-to-one relation). Only two galaxies (i.e., Au17 and Au23) show a mild displacement from the one-to-one relation, being characterized by higher central stellar mass density in Superstars than in L4. This might explain their, on average, lower $\langle A_1 \rangle$ measured in Superstars than L4 (see Fig. B.1), consistent with previous works that found a strong dependance of the lopsided amplitude on the central stellar mass density of the galaxies (Fontirroig et al. 2025).

Overall, these results show that the implementation of the Superstars method to improve the stellar particle mass resolution with respect to that of the gas cells does not significantly affect the overall stellar mass distribution (i.e., lopsidedness) within the galactic stellar disk, nor the central stellar mass density of the galaxy. In Sects. 3.3.1, 3.3.2, and 3.4.1, we use these results to expand the Superstars galaxy sample by including the L4 disk galaxies (i.e., with D/T > 0.45) that are not modeled with Superstars, thereby improving the statistical significance of the correlations between global galaxy properties.

Appendix C: Temporal evolution

In this section we present maps of the stellar and HI density distributions at consecutive output times for three of the Superstars galaxies discussed in Sect. 4. The corresponding lookback time is indicated in each panel.

We first highlight Au25 (Fig. C.1, Sect. 4.1), which is an example of a tidally induced lopsided perturbation in both its stellar and HI components, triggered by an interaction with a massive satellite within the last 1 Gyr. Similarly, Au6 (Fig. C.2, Sect. 4.1) shows a recent peak in lopsidedness across both its stellar and HI components at ∼1.5 Gyr. This was likely caused by the disk responding to a dark matter halo perturbed by the fly-by of a massive satellite. Finally, we show Au23 (Fig. C.3, Sect. 4.2), which experienced gas accretion from a fly-by satellite at early times (∼6 Gyr ago). This event induced lopsidedness in the HI gas while leaving the stellar component unperturbed (top panels of Fig. C.3). Subsequently, a further interaction with another massive satellite at ∼4 Gyr ago perturbed both the stellar and HI distributions (bottom panels of Fig. C.3).

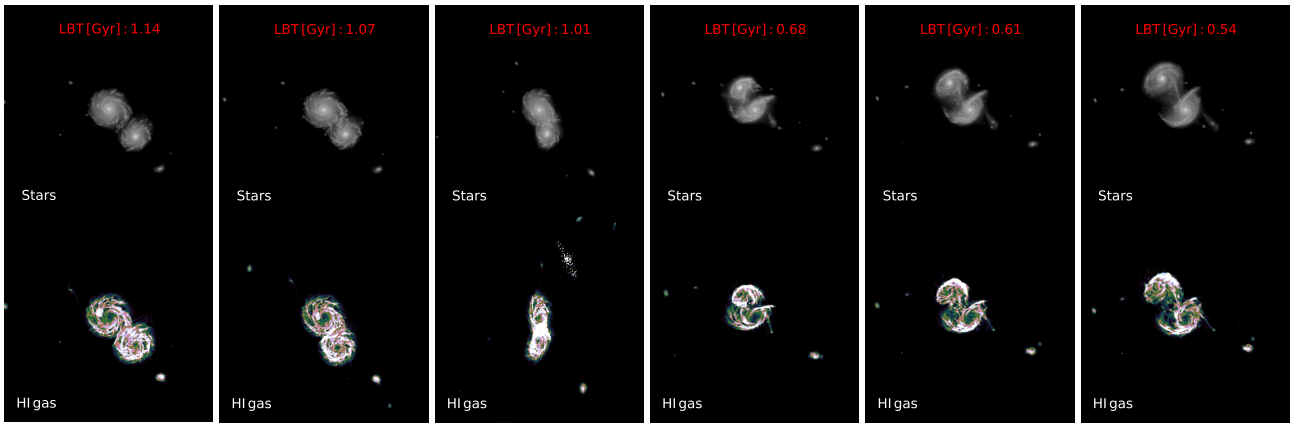


Fig. C.1. Au25: Snapshot sequence of the significant recent interaction experienced with a massive satellite (i.e., total mass ratio: 1:4-1:3) over the last 1 Gyr, which produced the coherent perturbation in both the stellar and HI components, as shown in Fig. 8. The pericentric passage occurs at ∼1 Gyr ago consistent with the increase in the global lopsidedness $\langle A_1 \rangle$ of both tracers. The box length, centered on the main host galaxy, corresponds to twice the virial radius R_{200} at each output time. The panels are shown in order of decreasing lookback time, from left to right.

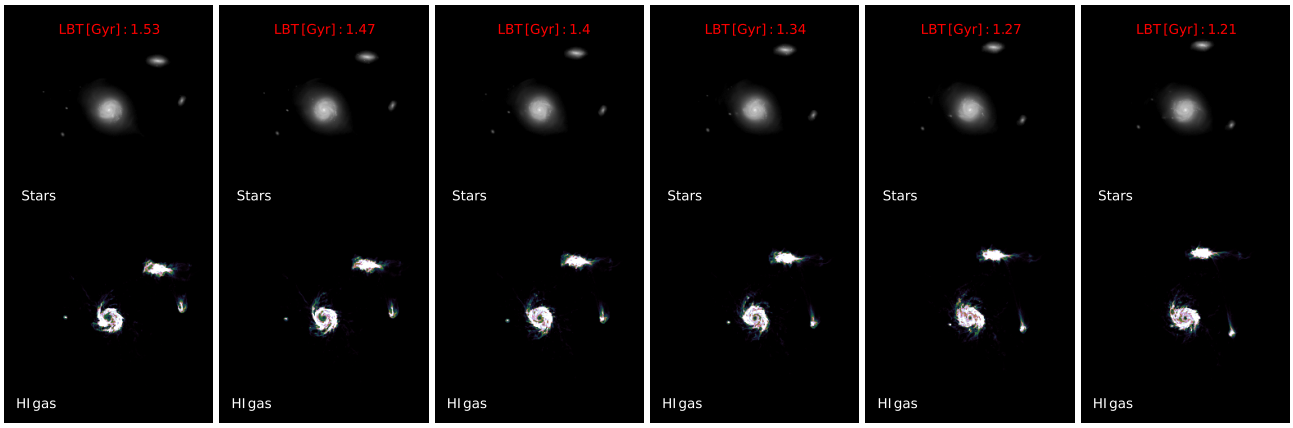


Fig. C.2. Au6: Snapshot sequence of the orbit of a massive fly-by satellite (i.e., total mass ratio: $\gtrsim$ 1:20). As shown in Fig. 8, the satellite never penetrates deeper than $0.5\,R_{200}$ and the pericenter is reached at ∼1.5 Gyr ago, consistent with the increase in the global lopsidedness $\langle A_1 \rangle$ of both the stellar and HI components. The box length, centered on the main host galaxy, corresponds to twice the virial radius R_{200} at each output time. The panels are shown in order of decreasing lookback time, from left to right.

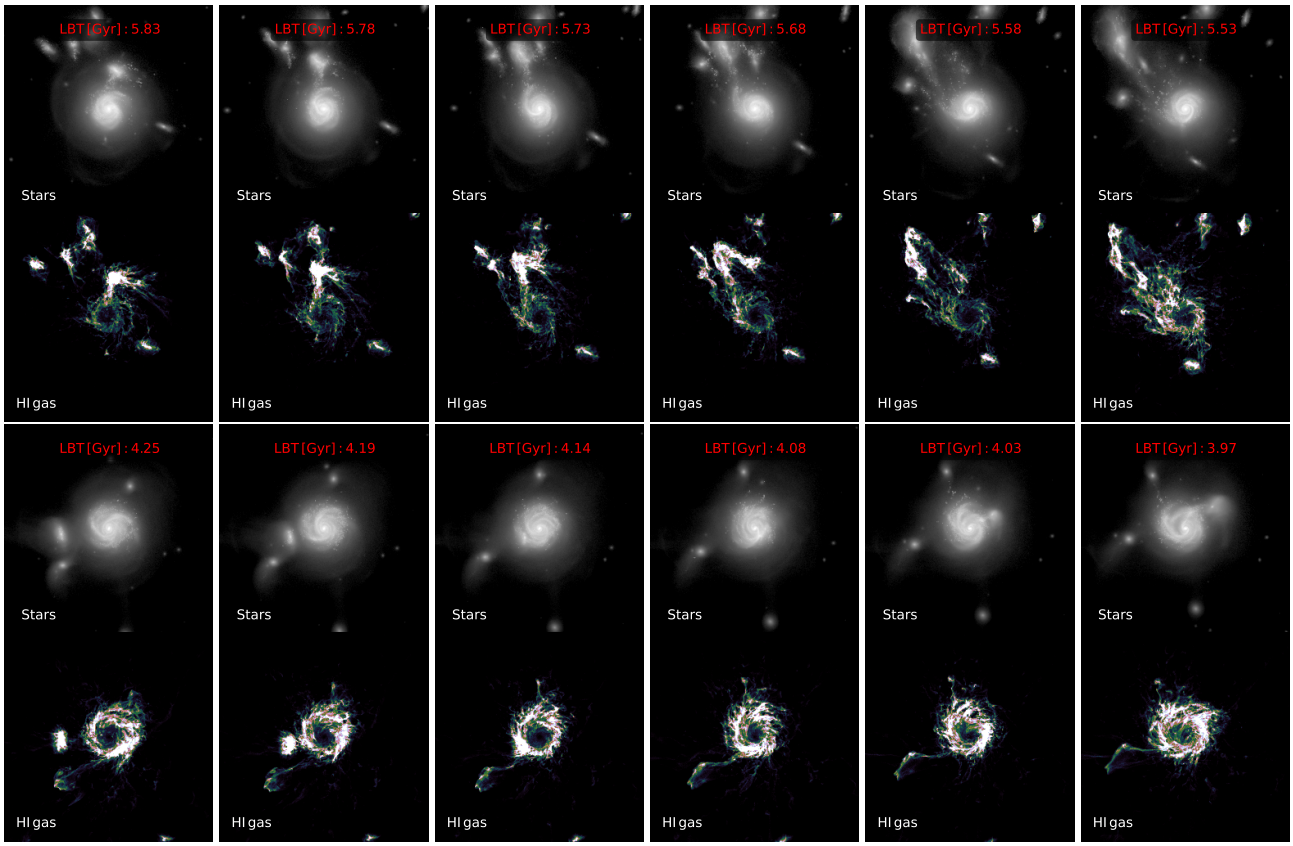


Fig. C.3. Au23: Snapshot sequence showing the early smooth gas accretion from two gas-rich fly-by satellites at ∼6 Gyr ago (*top panels*) and the subsequent significant interaction experienced with a massive satellite (total mass ratio ∼1:10) during its pericenter passage at ∼4 Gyr ago (*bottom panels*). As shown in Fig. 8, the former event only perturbed the HI component, while the latter perturbed both the stellar and HI components. The box length, centered on the main host galaxy, corresponds to one virial radius R_{200} at each output time. The panels are shown in order of decreasing lookback time, from left to right.

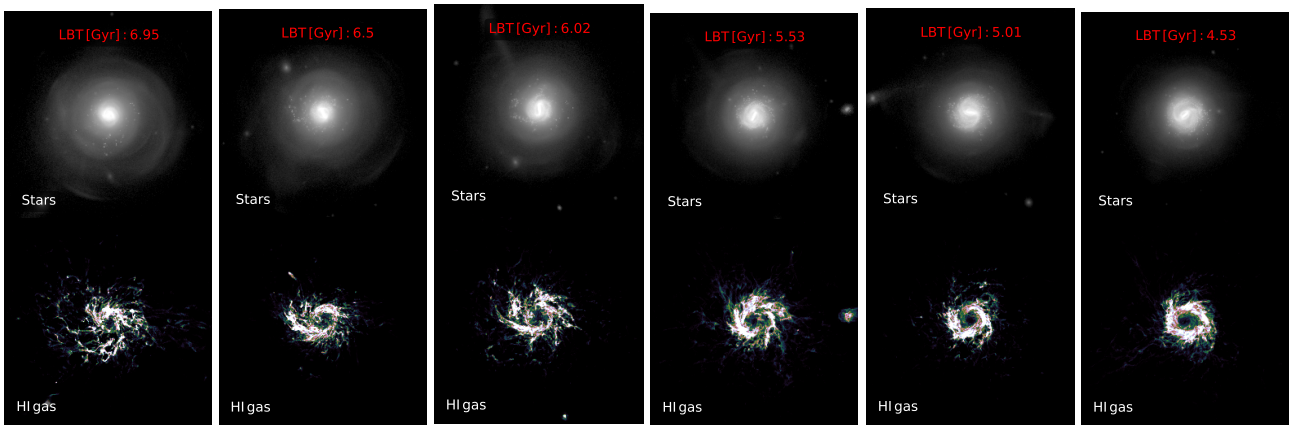


Fig. C.4. Au17: Sequence of six snapshot showing the time evolution between 4 to 7 Gyr ago for Au17, which belongs to the group of galaxies exhibiting only an early perturbation in the HI gas density distribution ($\gtrsim$ 4 Gyr ago) while maintaining an overall symmetric stellar disk throughout their evolution (see Fig. 8). As shown in Fig. 8, this galaxy did not experience any significant interactions with any massive satellite at early times (i.e., $\gtrsim$ 4 Gyr ago). It only experienced a fly-by passage from a low mass satellite (i.e., mass ratio of ∼1:50) at ∼2 Gyr ago, which did not cause significant perturbations to the stellar or HI gas disk. The box length, centered on the main host galaxy, corresponds to one virial radius R_{200} along each axis at each output time. The panels are shown in order of decreasing lookback time, from left to right.